

1 **Response to reviewers comments**

2 We thank the reviewers for their comments. Below we detail our responses (in red) to each point raised.
3 Changes to the revised ms are listed in blue.

4

5 **1. Community Comment by Bill Lanyon**

6 Fault plane properties for United Downs case

7 The cohesion and frictional properties used describe the strength of intact rock specimens (from Elliott
8 1984). It seems very unlikely that a fault / fracture plane would have significant cohesion. Wouldn't it be
9 more reasonable to assume only frictional strength for fault planes?

10 **In general we agree, a fair point. However, in terms of the overall model for fracture susceptibility, we think
11 it is useful to include cohesion as a variable. We can run models for cohesion set to 0 to address this issue.**

12 **In terms of the fault zone itself, we haven't seen cuttings or core from the boreholes, nor outcrops of the
13 PFZ. So we don't know if this fault zone is best characterised in terms of fault core + fault damage, with
14 gouge and cataclasite in the core; or, if it is better considered as a fracture corridor of pre-existing joints
15 and veins. In the latter case, we might expect some, albeit small, cohesive strength (perhaps a few kPa). In
16 the former case, "strength" would be better captured as frictional strength. But there would then be a
17 dynamic aspect to that, beyond the simple Mohr-Coulomb analysis we have used (e.g., experimental
18 evidence for frictional strength increasing with longer hold times between slip events).**

19 **In the case of zero cohesion, the comments we make still stand: that our knowledge of friction coefficients,
20 and especially their statistical distribution - skewed high or low - could be better.**

21

22 I agree that it's potentially useful to keep cohesion in the formulation but using the intact rock values is just
23 going to significantly overestimate the fault plane strength at low normal stress. I don't think much data
24 has been released from the UD deep borehole yet, but for mechanical properties there's only side-wall core
25 and chippings both of which might be quite limited in providing frictional properties for fault planes at
26 seismic scales. The image logs probably give some guide as to the structure. So while it's nice to get more
27 data there will still be a lot of expert judgment on fault plane frictional properties that go into a pfs model
28 and "caution" is probably going to lead to using zero cohesion in many cases.

29 **OK, agreed.**

30

31 There is now some published information on the PTF at the UD site in a paper from Reinecker et al. in
32 Geothermics.

33 **We have read this paper and cite this in our ms.**

34 **Lines 394 and 397.**

35

36 **Response to Reviewer 1 – Jonathan Turner**

37 We thank the reviewer for their comments (repeated below in black) and provide detailed responses below
38 (in red).

39

40 This paper addresses a topic of general societal interest; it is well written, carefully explained, thoughtful.
41 The paper highlights the importance of several fault zone processes which are previously known about but
42 this study provides fresh perspective e.g. the role of uncoupled fluid pressure, coupled fluid pressure
43 (poroelasticity), the frictional properties of fault rocks (gouge, cataclasites), the importance of optimally
44 constraining in situ stress measurements, etc. In fact I think poroelasticity deserves wider discussion here
45 and elsewhere because it may be the key to understanding the unpredictability of induced seismicity.

46 We are pleased that the ms is considered to be well written, carefully explained and thoughtful.

47
48 I have few substantive comments and recommend that this paper be published.

49 Thank you.

50
51 1. It may be a bit too long with a little too much space devoted to explaining the method (or perhaps
52 consider cutting one of the two synthetic case studies).

53 OK, fair point (also made by Reviewer 2 – Anon). We will delete the Manchester coalfield case study and
54 focus on United Downs deep geothermal for fracture susceptibility and South Wales coalfield shallow
55 geothermal for slip tendency.

56 Section 3.2

57
58 2. Rangely oil field, Colorado is another good example to cite of a case study which showed a critical
59 threshold in fluid pressure, above which seismicity was induced and below which it was absent (sorry, I
60 don't have the reference but I think it was in the 1970s).

61 Good point. We will include this seminal study in our background and/or discussion.

62 Line 62.

63
64 3. The Townend & Zoback dataset is intriguing but in my experience very difficult to apply to development
65 projects. What I mean is that it is hard to demonstrate that critically stressed faults are
66 conductive/transmissive/higher perm, at least in as clearly as the T & Z dataset shows they should be.

67 Agreed. But tackling this is beyond the scope of our ms.

68
69 4. I got confused by the difference between slip tendency and friction coefficient – in words, friction
70 coefficient is the ratio of shear force to tractional force at the moment of failure. So I then thought it's no
71 surprise that your modal slip tendency in the first case study is 0.56 because that's the inverse tan of
72 ~30degree which is an 'average' angle of internal friction for compacted rocks. I would find it useful if this
73 point could be explained in slightly more detail.

74 Our understanding is that slip tendency is a feature of the stress field and the fault plane orientation (shear
75 stress/normal stress), whereas friction is a rock property (an empirical measurement from laboratory
76 tests). So if slip tendency exceeds friction, then a fault slips; if slip tendency is less than friction, there is no
77 slip.

78 The friction coefficient will vary for different lithologies, different fault rocks, slip rates, etc. So for recently
79 formed faults in the present day stress field, slip tendency ought to be about 0.6-0.85 (Byerlee). But that
80 does not have to be the case for “old” faults formed under different stress states, not least because the
81 orientation of the present day in situ stress is not the one at the time of faulting (e.g., Carboniferous or
82 Permian in the case of the UK coalfields).

83

84 **Response to Reviewer 2 – Anonymous**

85 We thank the reviewer for their comments (repeated below in black) and provide detailed responses below
86 (in red).

87

88 First of all, I would say that the authors are top scientists in this field and accordingly, the idea and the
89 methodology reported in this paper seem to be very promising. Moreover, for people like me with a
90 prevalent geological background, the pure statistical part of the paper can be hard to be read just because
91 of the background.

92 Thanks. One key aim of our ms (see lines 52 – 59) is to explain the underlying theory and statistical
93 background to the Response Surface Methodology for just these reasons. And according to Reviewer 1, it is
94 “well written, carefully explained and thoughtful”.

95 No change.

96

97 However, the geological data seems to be, in my opinion, poorly exposed here and the statistics are
98 sometimes completely detached from the geological data making this paper quite difficult to be read from
99 a Solid Earth reader.

100 We don't understand what is meant by “geological data seems to be ... poorly exposed here”. We have
101 used the publicly available geological data for each case study, and cited all the sources.

102 Also, we do not understand the comment “the statistics are sometimes completely detached from the
103 geological data”. In the absence of complete certainty in the available data, we have used specific statistical
104 distributions to model the consequences of uncertainty.

105 No change.

106

107 Generally speaking, the paper faces a very interesting problem, and the method is innovative and very
108 exciting. As far as I can see the methodology is new and for this it must be tested and verified yet. The
109 authors attempt to do this by presenting two case studies with the aim to show “how combined RSM/MC
110 approach can be used to estimate the probability of slip on one or more faults”.

111 We agree that this is interesting, innovative and exciting.

112 No change.

113

114 However, the two cases are not very well constrained in terms is of boundary conditions making the
115 probability estimation quite confused.

116 We do not understand what the reviewer means by “boundary conditions”. We are not conducting a
117 numerical modelling analysis of a fixed spatial or temporal domain, e.g., of tensor fields or conservation
118 equations using finite differences, and therefore the notion of formal boundary conditions is misplaced, in
119 our opinion.

120 Our analysis, described in the first two sections, focuses on modelling the consequences of uncertainties in
121 all of the possible input parameters involved in the quantification of fault stability (using either fracture
122 susceptibility and slip tendency). As such it is a direct extension and development of the work presented by,
123 for example, Chiaramonte et al. (2008) and Walsh & Zoback (2016). We do not think the probability
124 estimation is “quite confused” (cf., comments by Reviewer 1).

125 No change.

126

127 Moreover, the two performed analyses (Porthtowan Fault Zone in Cornwall, UK and Coalfields in South
128 Wales and Greater Manchester, UK) differ in so many aspects and, more importantly the presented results
129 are different in terms of delivered outputs. This make the reading quite confusing and at the end of the
130 paper I got lost about the point that the authors would like to address. In my opinion to test a new
131 methodology we should apply this in areas where data are known as much as possible to see if the model
132 prediction are reliable. In this case since the two areas are poorly constrained, this exercise is difficult to be
133 followed and the results even more difficult to be understood.

134 We agree the case study areas are different, and the chosen modelled outputs are also different. This is all
135 deliberate. Our intention is to demonstrate the scope of the method (combined RSM and MC) to make
136 useful predictions about fault stability in terms of fracture susceptibility (United Downs) and slip tendency
137 (coalfields) in the face of uncertainty.

138 As noted above in Response to Reviewer 1, we will remove the Manchester coalfield case study to reduce
139 the length of the ms. We hope this makes it easier to appreciate the differences – and more importantly,
140 the value in those differences – in the two case studies.

141 In relation to “we should apply this in areas where data are known as much as possible to see if the model
142 prediction are reliable”: we know of no such datasets. In the case of United Downs – arguably one of the
143 best constrained sites involved in geothermal energy – all of the data remain uncertain (to varying
144 degrees), and this is one of our key points: even for areas with apparently “good” data, we argue that the
145 existing uncertainties are significant and have consequences.

146 Section 3.2 has been reduced.

147

148 The discussion paragraphs more than discuss the results present a list of what we should know to better
149 assess the seismic risk and the main message seems to be that we would need to know a lot of things. I can
150 kind of agree with this but, once again, this makes the main message of the paper more confused.

151 We disagree with this comment and agree with Reviewer 1 that the ms is “well written, carefully explained
152 and thoughtful”.

153

154 I strongly suggest the authors to simplify the paper in two ways.

- 155 1. Try to organize a sort of sensitivity analysis of the involved parameters in a more
156 structured and ordered way in order to facilitate the reader
- 157 2. Focus in one area and compare the results with something actually observed.

158 For the first point, sensitivity analyses are already included in the worked examples and in the case studies;
159 for example, we use CDF plots to explore the absolute sensitivity to selected parameters and we use
160 tornado plots to rank the relative sensitivities (see Figures 4, 5, 7 & 8).

161 For the second point, we think the reviewer might have missed the point. We know of no site or area
162 where the observations are known perfectly, i.e. with 100% certainty.

163 No change.

164

165 I think that we all agree that there are many topics related to the risk assessment (fault length, roughness,
166 friction, fluids, background seismicity, regional strain rate, and many many others) but in doing this exercise
167 authors must clearly state the assumption and critically analyze the results. In this paper I had the
168 impression that speaking about the many variables we lose the point of the paper, I would say that
169 sometimes less is more.

170 We have stated the assumptions used throughout (e.g., Mohr-Coulomb failure), and we critically analyse
171 the results through detailed statistical analysis of the outputs. One of our main aims, clearly listed in the
172 Introduction, is to provide a clear and detailed explanation of the method (in our opinion, so far lacking in
173 previous publications using similar methods). This entails some detailed and “careful explanation”
174 (Reviewer 1).

175 No change.

176

177 Minor points:

178 I am not so convinced about the statistical discussion that is sometimes too focused on the pure statistics
179 and few on the geology behind. For example, can we find a geological meaning to the “asymmetrical or
180 skewed” distribution of some parameters?

181 This is one of the issues raised by our ms, and clearly discussed! By trying to accommodate the fact of
182 uncertainty in all input parameters – stresses, orientations and rock properties – we are faced with making
183 choices about the nature (shape) of their distributions. We clearly state that there is currently insufficient
184 published data for many of these parameters – especially some critical ones such as cohesion and friction –
185 to find any “geological meaning”.

186 No change.

187

188 I Am not expert on Response Surface Methodology (RSM). However, the paragraph Statistical analysis of
189 geomechanical fault stability start with a discussion on the governing equations for RSM following a quite
190 long description that ends with the definition of Ts by meaning of the very well-known direction cosines
191 (e.g. Ramsay and Lisle 2000). In other word I can't really see why the authors need introducing the RSM
192 theory to infer the Ts definition.

193 The reviewer has perhaps missed the point. We are not “inferring” the Ts definition. The equations for Ts
194 are given in their full format (i.e., in terms of direction cosines) to highlight one of the key issues: there are
195 8 input parameters, and they are all, in general, uncertain. This is picked up in the succeeding paragraph
196 (line 221 in the original ms). We need to show the full equation for Ts before we make this crucial point.

197 No change.

198

199 A lot of acronyms BGS, CDF, are used but not defined. Even if they are quite easily understandable, this
200 gives the impression of a lazy writing

201 We presume the reviewer means “acronyms”. BGS is the British Geological Survey – we will add a definition
202 for that. CDF is defined on first use, on line 138.

203 BGS is now defined on first use in the main text, line 408.

204

205 The discussion on the relationship between fault length and events magnitude starts with this and ends
206 with discussing the relationship between fault length and number of events. I would say that the two
207 (maximum magnitude and number of events) are surely correlated but they are not the same thing.

208 Agreed. But we do not say they are the same thing.

209 No change.

210

211 Line to line comments:

212 Line 228 I would say that fluid pressure also influences Ts (e.g. De Paola et al., 2007)

213 We strongly disagree. Pore fluid pressure plays no part in the formal definition of slip tendency (Ts) – see
214 Morris et al., 1996. Moreover, the influence of pore fluid pressure on the potential for failure is better
215 understood in terms of fracture susceptibility – i.e., the pore fluid pressure increase needed to drive the
216 stress state on the fault to failure (Streit & Hillis, 2000).

217 No change.

218

219 Line 239 is CDF the cumulative distribution function? Authors should state this somewhere.

220 Yes it is. It is defined on first usage, on line 138 of the original ms.

221 No change.

222

223 Line 326 alfa has been not defined

224 Definition for alpha (α) will be added.

225 Now defined on first use, line 327.

226

227 Line 698 Why these may be the ones most likely to slip?

228 We are highlighting the *possibility* that unmapped (i.e., unknown) faults *may* be most likely – due to all the
229 factors discussed in this paper. The point is about unmapped faults, or so-called “known unknowns”.

230 No change.

231 Line 700 Some of this “mismatch” could be explained by the dip of the faults measured at the surface, but
232 not all. What the author mean here?

233 We mean that the surface traces of the faults shown on our maps may not coincide with their extension at
234 depth, e.g., for faults that dip at less than 90 degrees. This could explain some of the apparent mismatch
235 between the recorded earthquake locations plotted on the map relative to the surface traces.

236 No change.

237

238 Line 742 The observational record shows that bigger fault zones. I would say that there are a lot of physical
239 reasons behind this. Moreover, empirical relationships such as those suggested by Wells and Coppersmith
240 1994, or Leonard 2010 should be cited here.

241 Thanks for these suggestions. We will add these papers.

242 Line 810.

243

244 Subsequent comments and replies...

245 I read the answers to my comments, and I have to say that I really hope that the Editor and all the SE
246 readers will find the whole paper “well written, carefully explained and thoughtful” . I still think that some
247 parts should be improved, however I just reported my suggestions hoping to help.

248 In any case, I would like just to comment on the answer regarding T_s dependence on fluids.

249 The answer was:

250 We strongly disagree. Pore fluid pressure plays no part in the formal definition of slip tendency (T_s) – see
251 Morris et al., 1996[...].

252 In the Morris et al paper T_s is defined by τ/σ . σ are, generally speaking, the principal stresses
253 that might be interpreted as fluid pressure independent because effective stresses are not mentioned.
254 However, in the same paper, Morris et al., 1996 calculated the T_s for the Yucca Mountain area and, while
255 setting the input σ , the literally write:

256 [...] to a depth of 5 km and assuming an average rock density of 2.7 g/cm³, $s_1 = 133$ MPa, $s_2 = 58$ – 108
257 MPa, and $s_3 = 63$ – 72 MPa. Assuming a water-table depth of 600 m (Stock et al., 1985), and
258 interconnecting permeability hydrostatic pressure at 5 km will be 43 MPa. Thus, effective principal stresses
259 would be: $s_1 = \text{vertical} = 90$ MPa, $s_2 = N258E-N308E = 45$ – 65 MPa (50%–72% of s_1), and $s_3 = N608W-N658W$
260 = 20–29 MPa (22%–32% of s_1), at 5 km beneath Yucca Mountain.

261 Please note that the effective stresses are those used by Morris et al., in their calculation of T_s (Figure 3).
262 This is also confirmed by Lisle and Srivastava, 2004 that literally write: “If pore-fluid pressures are involved,
263 then the stresses should be considered effective stresses.”

264 If effective stresses should be used, T_s would change with changing P_f , also because τ is Pore-pressure
265 independent. I would say, thus, that I “strongly” believe that T_s does depend on P_f .

266 What can be independent from P_f is the $T_s/T_{s\max}$ ratio (defined as “ T ’s” by Lisle and Srivastava, 2004).
267 However, T_s and not T ’s is investigated in the present paper by Healy and Hicks.

268

269 Thanks again for the comments.

270

271 We agree that the formal definition of slip tendency does not include pore fluid pressure. The question
272 then is: is it useful to modify the normal stress term by subtracting the pore fluid pressure to get an
273 'effective normal stress', and an 'effective slip tendency'.

274

275 In our opinion, the power of the original definition of Ts is how it can be related to the friction coefficient at
276 the fault surface. That is, the slip tendency, a function of the stresses on the fault plane, can be compared
277 to the rock properties (the friction coefficient), and an assessment of stability can be made. It is not clear
278 how this works for 'effective' terms. Effective friction?

279

280 Therefore, to clearly separate potential frictional processes from hydraulic (pore fluid pressure) processes,
281 we believe it is better to keep the original definition of slip tendency, and use fracture susceptibility as an
282 index of stability under effective pressure/stress.

283 No change.

284

285 **De-risking the energy transition by quantifying the uncertainties in fault stability**

286 David Healy¹ & Stephen P. Hicks²

287 ¹School of Geosciences, University of Aberdeen, Aberdeen AB24 3UE United Kingdom

288 ²Department of Earth Science and Engineering, Imperial College, London SW7 2AZ United Kingdom

289 d.healy@abdn.ac.uk

290

291 **Abstract**

292 The operations needed to decarbonise our energy systems increasingly involve faulted rocks in the
293 subsurface. To manage the technical challenges presented by these rocks and the justifiable public concern
294 over induced seismicity, we need to assess the risks. Widely used measures for fault stability, including slip
295 and dilation tendency and fracture susceptibility, can be combined with Response Surface Methodology from
296 engineering and Monte Carlo simulations to produce statistically viable ensembles for the analysis of
297 probability. In this paper, we describe the implementation of this approach using custom-built open source
298 Python code (*pfs* – probability of fault slip). The technique is then illustrated using two synthetic datasets and
299 two case studies drawn from active or potential sites for geothermal energy in the UK, and discussed in the
300 light of induced seismicity focal mechanisms. The analysis of probability highlights key gaps in our knowledge
301 of the stress field, fluid pressures and rock properties. Scope exists to develop, integrate and exploit citizen
302 science projects to generate more and better data, and simultaneously include the public in the necessary
303 discussions about hazard and risk.

304

305 **Introduction**

306 *Rationale & Objectives*

307 Faults in the crust slip in response to changes in stress or pore fluid pressure, and the source of these changes
308 can be either natural or anthropogenic. Estimating the likelihood of slip on a particular fault for a given
309 change in loading is critical for the industrial operations of the energy transition, especially geothermal
310 energy and carbon sequestration and storage (CCS). The target formations of these operations are nearly
311 always faulted and fractured to some degree, and experience from waste-water injection in the USA shows
312 how even small changes in pore fluid pressure can trigger frequent seismic slip on these faults, with
313 significant and widespread impact on society (e.g., Elsworth et al., 2016; Hincks et al., 2018; Hennings et al.,
314 2019).

315 Stephenson et al. (2019) have shown how quantitative analysis of the subsurface is one of the key
316 contributions that geoscientists can make to decarbonising energy production to meet national and
317 international targets (e.g., CCC, 2019; IPCC, 2018). This includes the systematic geomechanical
318 characterisation of rock formations, better understanding of fluid flow in fractured rocks, and the need for
319 pilot projects to explore the scaling of behaviours from the laboratory to the field. Perhaps the most
320 important aspect is to understand the public attitudes to subsurface decarbonisation technology
321 (Stephenson et al., 2019; Roberts et al., 2021). Several recent studies have addressed the uncertainties in
322 subsurface structural analysis of faulted rocks (Bond, 2015; Alcalde et al., 2017; Miocic et al., 2019). In this
323 paper, we extend this work to specifically include fault stability, and argue that in order to simultaneously
324 address public concerns and assess the viability of different schemes, we need a more rigorous approach to
325 risking subsurface decarbonisation activities, especially where these involve changes in load on faulted rocks.

326 Useful measures of fault stability include slip and dilation tendency (T_s and T_d respectively) and fracture
327 susceptibility (S_f , the change in fluid pressure to push effective stress to failure). These measures are defined
328 as functions of the *in situ* stress, the orientation of the fault plane and, in the case of S_f , rock properties. It is
329 widely recognised that the inputs for the prediction of stability are always uncertain, and to varying degrees:
330 e.g., the vertical stress component of the *in situ* stress tensor can often be quite well constrained (to within

331 5%) from density log data, whereas the maximum horizontal stress is generally much harder to quantify. To
332 improve and focus our predictions of fault stability in the subsurface, we need to accept and incorporate
333 these uncertainties into our calculations. In this paper, we describe and explore a statistical approach to fault
334 stability calculations, and then apply these methods to examples in geothermal energy, in both low- and
335 high-enthalpy settings.

336 The specific aims of this paper are to:

- 337 1. describe and explain the Response Surface Methodology, and show how it can be applied to the
338 probabilistic estimation of fault stability using a range of different measures;
- 339 2. explore how the main variables – in situ stress, fault orientation and rock properties – relate to the different
340 measures of fault stability (T_s , T_d and S_f) using synthetic (i.e., artificial) data;
- 341 3. use case studies of active and proposed geothermal projects with publicly available data to illustrate the
342 method, and then highlight the relationships between our known but uncertain input data and the predicted
343 risk of fault slip.

344 *Importance & Previous work*

345 Small changes in stress or fluid pressure (e.g., a few MPa) from human activities can have significant
346 consequences for fault stability (Raleigh et al., 1976). For example, waste-water injection from hydraulic
347 fracturing (“fracking”) operations has led to dramatic increases in seismicity in Oklahoma since 2009 (Hincks
348 et al., 2018) and in Texas since 2008 (Hennings et al., 2019; Hicks et al., 2021). The precise mechanical cause(s)
349 of this seismicity is the subject of some debate, and could be due to either ‘direct’ pore fluid pressure transfer
350 to basement-hosted faults leading to a reduction in effective stress, or ‘indirect’ poroelastic effects at a
351 distance (Elsworth et al., 2016; Goebel et al., 2019). The concept of critically stressed faults in the crust
352 (Townend & Zoback, 2000), where relatively high permeability serves to maintain near-hydrostatic pore
353 pressures, is consistent with the idea that only minor perturbations in loading can have dramatic
354 consequences, even in areas of apparently low seismicity and, implicitly, low background tectonic loading.

355 In densely populated areas such as the UK, public support for, and confidence in, subsurface operations are
356 key. Hydraulic fracturing operations for shale gas in Lancashire (UK) were stopped after earthquakes were
357 triggered by fluid injection (Clarke et al., 2019). Triggered felt seismicity has already been reported at the
358 United Downs deep geothermal pilot in Cornwall (Holmgren & Werner, 2021). Note that, in both of these
359 cases, fracturing and/or fault slip are intrinsic to the success of the operation as they are needed to enhance
360 fluid flow, and therefore earthquakes are inevitable. In detail, microseismicity (i.e., $M < 2$) is inevitable, but it
361 is important to understand whether felt (i.e. $M > 2$) seismicity can be forecast ahead of time. Furthermore,
362 many sites for energy transition projects in the UK are located in (beneath) areas of extreme poverty and
363 social deprivation, both rural (e.g., Cornwall, South Wales) and urban (e.g., Glasgow), and therefore the risks
364 from these projects fall disproportionately on the less well off (Nolan, 2016; McLennan et al., 2019). To begin
365 to address these complex issues, we need to quantify which faults are more or less likely to slip in response
366 to induced changes in loading. One approach is to analyse data during subsurface operations and attempt to
367 manage the consequences (e.g., Verdon & Budge, 2018). An alternative approach, and the one taken in this
368 paper, is to look at the bigger picture before operations commence and reduce risk from the outset.

369 Various measures have been proposed to quantify the propensity or tendency of a given fault to slip (or
370 open) in a known stress field. The following methods are based around an assumption of Mohr-Coulomb
371 (brittle-plastic) failure which has been shown to capture the key aspects of faulting in the upper crust. Slip
372 tendency (T_s) was introduced by Morris et al. (1996) and is the simplest measure of fault stability, defined as:

$$373 \quad T_s = \tau / \sigma_n \quad (1)$$

374 where τ is the shear stress and σ_n is the normal stress acting on the fault plane. These stress components in
375 turn depend on the principal stresses and the orientation of the fault plane (see Lisle & Srivastava, 2004 for
376 details). In the absence of cohesion, if the slip tendency on a fault equals or exceeds the coefficient of sliding
377 friction, then the fault can be deemed “unstable”. This dimensionless index embodies the key mechanical
378 principle underlying Mohr-Coulomb shear failure: as the shear (“sliding”) stress acting on a fault plane rises

379 in relation to the normal (or “clamping”) stress, the fault approaches failure and will slip. Slip tendency allows
 380 us to compare what we know about the stress state on a fault (τ , σ_n) with what we know about the rock
 381 properties (friction, μ). Dilation tendency (T_d) has been defined to describe the propensity for a fault to open,
 382 or dilate, in a given stress regime:

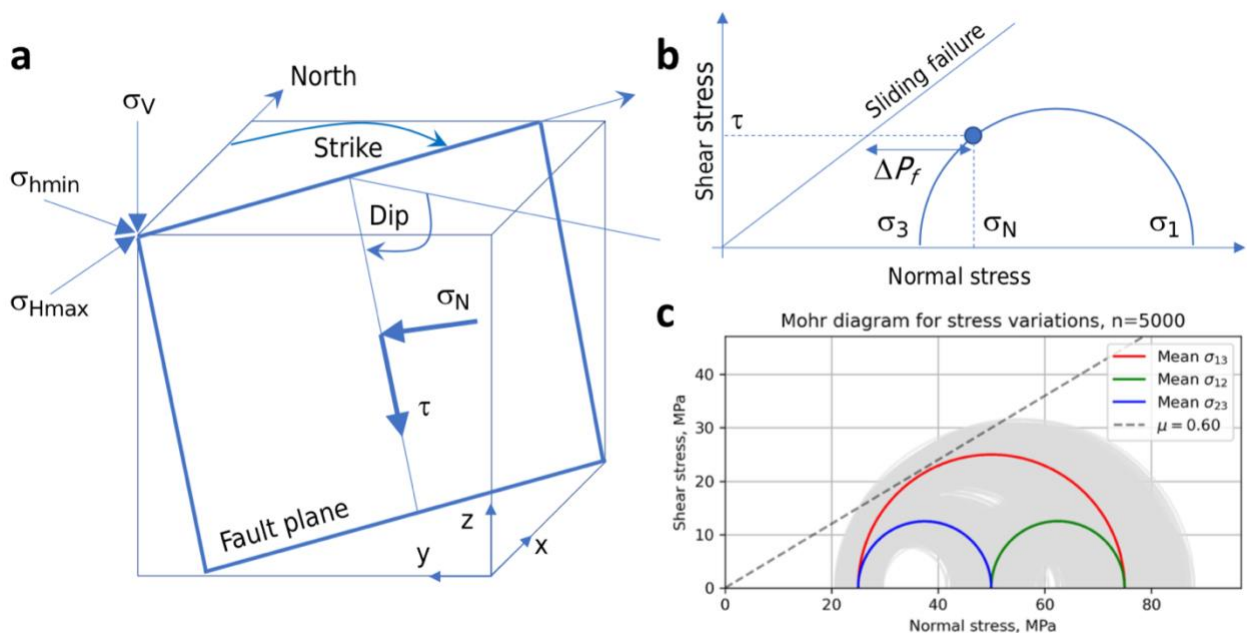
$$383 \quad T_d = (\sigma_1 - \sigma_n) / (\sigma_1 - \sigma_3) \quad (2)$$

384 where σ_1 and σ_3 are the principal stresses of the *in situ* stress tensor (Ferrill et al., 1999).

385 Most rocks in the upper crust are porous and permeable to some degree, and fault rocks are no exception,
 386 so these rocks are generally fluid saturated. This implies that we should include pore fluid pressure and the
 387 concept of effective stress in our assessment of fault stability. Fracture susceptibility (S_f) is the change in pore
 388 fluid pressure needed to push a stressed fault to failure (Streit & Hillis, 2004) and is defined by:

$$389 \quad S_f = \Delta P_f = (\sigma_n - P_f) - (\tau - C_0) / \mu \quad (3)$$

390 where P_f is the pore fluid pressure at the fault, C_0 is the cohesive strength (or cohesion), and μ is the
 391 coefficient of sliding friction (see Figure 1b).



392
 393 **Figure 1.** a. Schematic block diagram of a fault plane showing the terminology used in this paper. Also shown
 394 are the cartesian and geographic reference frames and the Andersonian principal stresses. b. Mohr diagram
 395 for a given state of stress (blue semi-circle) with normal (σ_n) and shear stresses (τ) marked for a selected fault
 396 plane orientation (blue dot). Failure envelope for frictional sliding (cohesion=0) also shown as straight blue
 397 line. c. Mohr diagram depicting one of the key issues tackled in this paper: given uncertainty in the input
 398 stress values (grey Mohr circles for the variation around the average principal stresses in red, blue and green),
 399 what is the probability of failure? i.e., what percentage of all these stress states will intersect the failure
 400 envelope?

401 Previous applications of these three measures of fault stability – T_s , T_d and S_f – cover the full spectrum of rock
 402 types and stress fields, from basins to basement and from extensional, contractional and wrench tectonic
 403 settings. Applications within the domain of the energy transition include examples from geothermal energy
 404 (both shallow and deep) and CCS. The original definition of fracture susceptibility by Streit & Hillis (2004) was
 405 concerned with safe injection limits for CO₂ in potential reservoirs in Australia. Moeck et al. (2009) used slip
 406 tendency to quantify the relative stability of different fault sets in different horizons in a geothermal reservoir
 407 in the North German Basin, and Barcelona et al. (2019) used a similar method for Copahue geothermal
 408 reservoir in Argentina. For CCS, Williams et al., (2016, 2018) have used slip tendency analyses of faults in
 409 potential sandstone reservoirs on the UK continental shelf, including the North Sea and East Irish Sea basins.

410 The links between subsurface fluid flow, seismicity, and fault stability have recently been explored by Das &
 411 Mallik (2020) for the Koyna earthquakes in India, and by Wang et al. (2020) for strike-slip faults in the Tarim
 412 Basin of China.

413 Probabilistic approaches to fault stability have been adopted by various workers. In risking CO₂ storage for
 414 an oil reservoir in the Williston basin, Ayash et al. (2009) used a features, events and processes (FEP)
 415 approach to constrain the likelihood of occurrence of fault slip (based on slip tendency) and the severity of
 416 the consequences, with their product defined as the risk. Rohmer & Bouc (2010) used RSM to assess cap rock
 417 integrity for tensile or shear failure above deep aquifers in the Paris basin targeted for the storage of CO₂.
 418 Coupled RSM and Monte Carlo approaches to fault stability have been used by Chiaramonte et al. (2008) and
 419 Walsh & Zoback (2016), following their initial application in the field of wellbore stability by Moos et al.
 420 (2003). This Fault Slip Potential (FSP) method developed by Stanford (e.g., Chiaramonte et al., 2008 & Walsh
 421 & Zoback, 2016) calculates the response surface for fracture susceptibility, with the in situ stress tensor
 422 calculated by inversion of abundant seismicity data (focal mechanisms), and then uses a Monte Carlo
 423 simulation to generate cumulative distribution functions (CDFs) of conditional probability of slip defined with
 424 reference to an arbitrary pore pressure perturbation ($\Delta P_f = 2$ MPa, in the case of Walsh & Zoback, 2016).
 425 Note that FSP assumes cohesionless faults ($C_0=0$) and hydrostatic pore fluid pressure, and that *conditional*
 426 probability in this sense refers to the fact that we do not know where any particular fault is with respect to
 427 the seismic cycle.

428 *Conventions and layout for this paper*

429 In the sections below, we describe the underlying equations for measuring fault stability and then show how
 430 we can use Response Surface Methodology (RSM) from engineering to explore the consequences of
 431 uncertainties in the input variables. After assessing the quality of the solutions obtained from RSM, we then
 432 apply a brute force Monte Carlo (MC) approach to generate cumulative distribution functions (CDFs) of the
 433 different measures (T_s , T_d and S_f). The case studies use published, publicly available data to constrain the
 434 input variable distributions and then a combined RSM/MC approach is used to explore the uncertainty in
 435 fault stability in different settings.

436 In this paper, compressive stress is reckoned positive, with σ_1 as the maximum compressive principal stress
 437 and σ_3 as the minimum principal stress. Stress states and fault regimes are assumed to be Andersonian, with
 438 one principal stress vertical, although the underlying model and code could be changed to incorporate non-
 439 Andersonian stress states with the addition of extra variables for the stress tensor orientation (Walsh &
 440 Zoback, 2016). The likelihood of slip on a fault is assessed in the framework of Mohr-Coulomb failure, with
 441 or without cohesion (Jaeger et al., 2009). Fault orientations are quantified as strike and dip, following the
 442 right-hand rule: with your right hand flat on the fault plane and fingers pointing down dip, the right thumb
 443 points in the direction (azimuth) of strike. The relationship between the geographical and cartesian reference
 444 frames follows a North-East-Down convention. Figure 1 depicts the key terms and elements used in the
 445 analysis, and Table 1 contains a list of terms and symbols used with units where appropriate.

Quantity	Symbol	Units
Maximum compressive stress	σ_1	MPa
Intermediate compressive stress	σ_2	MPa
Minimum compressive stress	σ_3	MPa
Vertical stress	σ_v	MPa
Maximum horizontal stress	σ_{Hmax}	MPa
Minimum horizontal stress	σ_{Hmin}	MPa
Azimuth of max. horizontal stress	$sHaz$	°
Pore fluid pressure	P_f	MPa
Coefficient of friction	μ	dimensionless
Cohesive strength (or cohesion)	C_0	MPa
Slip tendency	T_s	dimensionless
Dilation tendency	T_d	dimensionless
Fracture susceptibility	S_f	MPa

Fault strike	φ	°
Fault dip	δ	°
Shear stress on a fault plane	τ	MPa
Normal stress on a fault plane	σ_n	MPa

446

447 **Table 1.** List of terms and symbols used in this paper, with units where appropriate.

448

449 **Statistical analysis of geomechanical fault stability**

450 *Introduction to Response Surface Methodology (RSM)*

451 RSM is widely used in engineering and industry along with a Design of Experiments approach, and often
 452 employed to optimise a specific process of interest – e.g., to maximise the yield of a reaction given the input
 453 variables of pressure, temperature, reactant mass etc. RSM is a large and growing field and is best considered
 454 as a toolbox of different methods with a common mathematical basis. The governing equations for RSM were
 455 derived by Box & Wilson (1951). The core idea is that a response y can be represented by a polynomial
 456 function of a number (q) of input variables $x_1 - x_q$:

$$457 \quad y = f(x_1, x_2, \dots, x_q) \quad (4)$$

458 Each of the q input variables can be represented by either a discrete set of measurements made in the
 459 laboratory (or field) or drawn from appropriate statistical distributions (normal/Gaussian, skewed normal,
 460 Von Mises etc.). The simplest polynomial function that relates y and x is a linear one:

$$461 \quad y_i = \beta_0 + \beta_1 x_{i1} + \beta_2 x_{i2} + \dots + \beta_q x_{iq} + \epsilon_i \quad (5)$$

$$462 \quad y_i = \beta_0 + \sum_{j=1}^q \beta_j x_{ij} + \epsilon_i \quad (6)$$

463 where β_q are the coefficients (to be determined), y_i is the set of observations of the response ($i = 1, 2, \dots, N$),
 464 and x_{ij} are the input variables ($j = 1, 2, \dots, q$). ϵ is the experimental error, and the number of ‘observations’ N
 465 $> q$, the number of input variables. This is therefore a multiple regression model linking the response y to
 466 more than one (i.e., multiple) independent variables, x .

467 A more complex polynomial relationship is the quadratic form:

$$468 \quad y = \beta_0 + \sum_{j=1}^q \beta_j x_j + \sum_{j=1}^q \beta_{jj} x_j^2 + \sum_{i < j}^q \beta_{ij} x_i x_j + \epsilon \quad (7)$$

469 This 2nd order multiple regression model contains all the terms of the linear (1st order) model, but also extra
 470 terms for the squares and cross-products of the input variables (second and third terms on the RHS of
 471 equation 7).

472 To define a response surface, either linear or quadratic, we need to calculate the values of the β_q coefficients.
 473 We can rewrite the key equations in matrix form:

$$474 \quad \mathbf{y} = \mathbf{X}\boldsymbol{\beta} + \boldsymbol{\epsilon} \quad (8)$$

475 where \mathbf{y} is an ($N \times 1$) vector of observations (or calculations), \mathbf{X} is an ($N \times k$) matrix of input variable values (k
 476 $= q + 1$), and $\boldsymbol{\beta}$ is a ($k \times 1$) vector of regression coefficients. We solve this system of equations using the
 477 standard linear algebra technique of least squares regression (Myers et al., 2016):

$$478 \quad \hat{\boldsymbol{\beta}} = (\mathbf{X}'\mathbf{X})^{-1}\mathbf{X}'\mathbf{y} \quad (9)$$

479 The response surface (linear or quadratic) is then defined by

$$480 \quad \hat{\mathbf{y}} = \mathbf{X}\hat{\boldsymbol{\beta}} \quad (10)$$

481 The values used in \mathbf{X} are chosen to efficiently span the parameter space. A typical sampling design for \mathbf{X} is
 482 called the 3^q model with 3 values of each variable, usually the minimum, mean (or mode) and maximum. For

483 slip tendency, $q = 6$ and this means we use $3^q = 3^6 = 729$ data points to calculate the response surface. In
 484 practice, coded variables are used in \mathbf{X} where the absolute values for the minimum, mean and maximum of
 485 each variable are scaled to -1 , 0 and $+1$ respectively, and then scaled back when the response surface is used
 486 in the Monte Carlo simulation (Myers et al., 2016).

487 The response surface – i.e., the set of β coefficients – is defined using a limited number of sample points,
 488 depending on the chosen sample design (3^q in the examples used in this paper; other variants exist – see
 489 Myers et al., 2016 for details). To explore the possible variations of a response more fully, we use a Monte
 490 Carlo (MC) approach of pre-defined size ($N_{MC} = 5,000$ in the examples in this paper). The MC simulation uses
 491 the response surface calculated from the design points to calculate the responses for N_{MC} combinations of
 492 input variables drawn from their distributions. This produces a statistically viable ensemble of response
 493 values from which we can infer the probability of the response with respect to a chosen threshold.

494 With respect to fault stability, we can use RSM to produce a parameterised relationship – the response
 495 surface in q dimensions – between a stability measure of interest and the q input variables. In the case of slip
 496 tendency T_s , we can rewrite the components of equation 1 in terms of the measurable input quantities as
 497 follows:

$$498 \quad \tau = \sqrt{(\sigma_1 - \sigma_2)^2 l^2 m^2 + (\sigma_2 - \sigma_3)^2 m^2 n^2 + (\sigma_3 - \sigma_1)^2 l^2 n^2} \quad (11)$$

$$499 \quad \sigma_n = \sigma_1 l^2 + \sigma_2 m^2 + \sigma_3 n^2 \quad (12)$$

500 where l , m and n are the direction cosines of the normal (pole) to the fault plane given by

$$501 \quad l = \sin \delta \sin \phi \quad (13a)$$

$$502 \quad m = -\sin \delta \cos \phi \quad (13b)$$

$$503 \quad n = \cos \delta \quad (13c)$$

504 where ϕ is the fault strike and δ is the fault dip, in a North-East-Down reference frame (Allmendinger et al.,
 505 2012).

506 All terms on the right-hand sides of equations 11-13 are uncertain to some degree, therefore estimating the
 507 uncertainty of T_s , and as importantly, the *key controls on the uncertainty of T_s* , in terms of these input
 508 variables, is non-trivial. This difficulty in estimating and visualising possible variations in our estimates of T_s
 509 is exacerbated by the recognition that each of the input variables may be distributed differently: some
 510 quantities (e.g., the principal stresses) may follow normal (Gaussian) statistics, whereas others (e.g., strike,
 511 dip, sHmax azimuth) will follow Von Mises distributions. In the case of fracture susceptibility (S_f , equation 3),
 512 it is even more complicated with the addition of three further input variables for friction, cohesion and pore
 513 fluid pressure. Measurements or calculations of coefficients of friction and cohesive strength often display
 514 asymmetric or skewed distributions (skewed high or low), and this adds further complexity to the task of
 515 estimating and constraining fault stability from the data at hand.

516 *Worked Example 1: Slip tendency from synthetic input data*

517 The calculations presented in this paper were all performed with the custom pfs (**p**robability of **f**ault **s**lip)
 518 package, written by the first author (DH) in Python 3, and freely available on GitHub (see Code Availability,
 519 below).

520 The first example calculates a response surface for slip tendency (T_s) from $q=6$ input variables: the
 521 magnitudes of the three principal stresses of the *in situ* stress tensor (σ_1 , σ_2 , σ_3) assumed Andersonian with
 522 one principal stress vertical, the azimuth of the maximum horizontal stress (*sHaz*), and the strike and dip of
 523 the fault plane. This response surface is then used in a Monte Carlo simulation ($N_{MC} = 5,000$) to generate a
 524 CDF of T_s values for the fault. The specific Python code to run this example in the pfs package is wrapped in
 525 a Jupyter notebook available on GitHub (WorkedExample1.ipynb).

526 The first task is to define the distributions of the input variables. In pfs, examples are shown for normal,
 527 skewed normal and Von Mises (circular normal) distributions, but other statistical distributions are allowed.

528 Table 2 and Figure 2 describe the ranges and moments of these distributions for each input variable. For this
 529 example, the normally distributed principal stresses are defined with a variation (standard deviation) of 5%
 530 of their central (mean) value, and the Von Mises distributions of the azimuthal variables (sHaz, strike and dip)
 531 all have $\kappa = 200$ to model their dispersion about their mean. The fault of interest strikes 060° and dips 60° to
 532 the south (right hand rule). The key questions to be addressed by this example are:

- 533 1. given these uncertainties in the input stresses and orientation data, how does the estimation of T_s
 534 vary? What is the range and the mode?
- 535 2. which variables exert the greatest (and least) control on the predicted variation in T_s ?

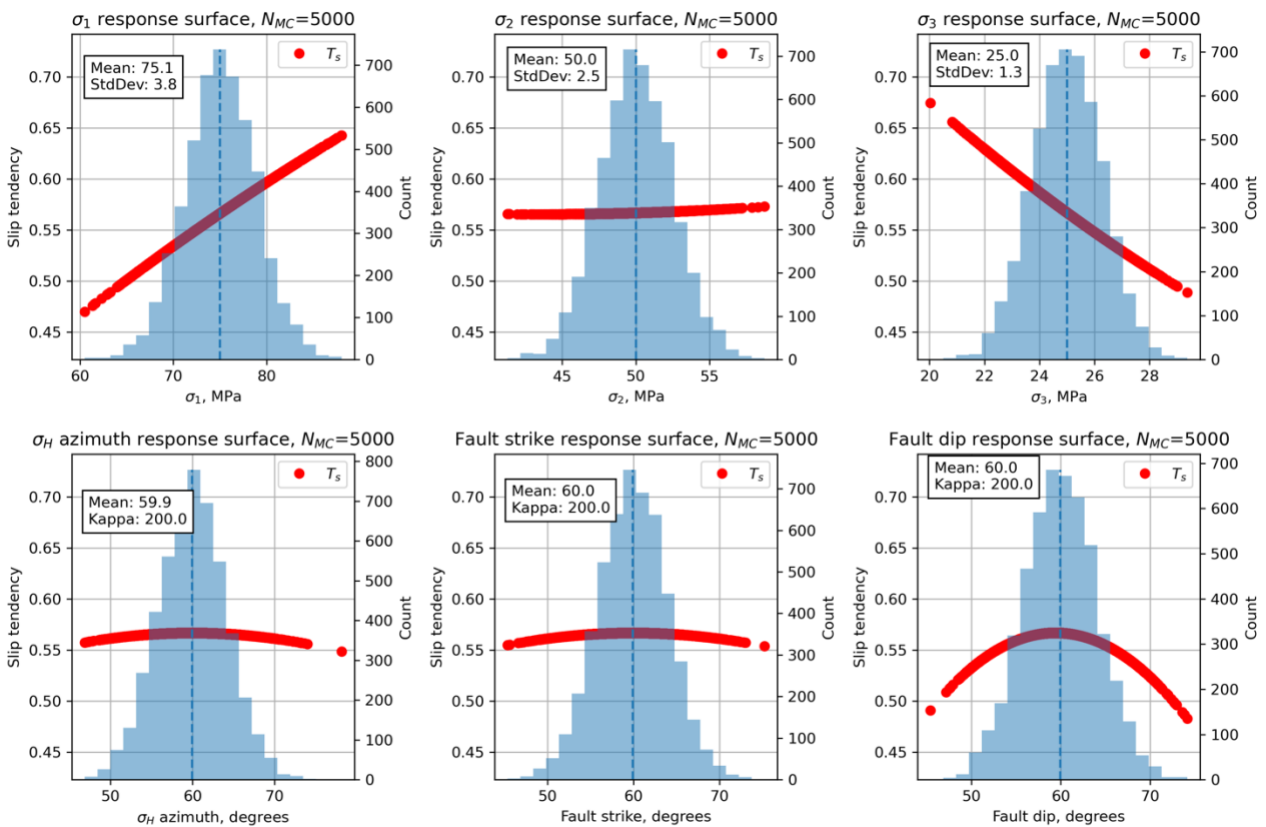
536 We first build a response surface using a 3^q design, i.e., 3 data points for each variable – minimum, mean and
 537 maximum – and for T_s , $q = 6$. This means we calculate the response surface from $3^6 = 729$ data points. We
 538 compare a calculated linear response surface with a quadratic response surface, using a normal probability
 539 plot of residuals (Figure 3). These residuals are the differences between the values of T_s derived from the
 540 observations (taken from the input distributions shown in Table 2 (upper) and Figure 2), and the calculated
 541 values of T_s using the β coefficients derived by least squares regression i.e., the response surface. The
 542 adjusted R^2 value for the quadratic 2nd order model is significantly better than that for a linear 1st order model,
 543 and we use quadratic models throughout the rest of this paper. More detailed inspection of the quality of fit
 544 between the response surface and the observations is possible, including analysis of variance, main effects
 545 plots and the use of t-statistics for each input variable to quantify their significance to the definition of the β
 546 coefficients (Myers et al., 2016). In practice, visualising sections of the response surface for individual
 547 variables is generally sufficient (see below; Moos et al., 2003; Walsh & Zoback, 2016).

Variable	Mean	Standard deviation (κ for Von Mises)	Units	Distribution	Comments
Worked Example 1 – Synthetic T_s – modelled depth=3 km					
σ_v , vertical stress	75.0	3.75 (5% of mean)	MPa	Normal	Lithostatic for depth of 3 km, assuming average rock density of 2500 kg m^{-3}
σ_H , max. horizontal stress	50.0	2.5 (5% of mean)	MPa	Normal	Andersonian normal faulting regime
σ_h , min. horizontal stress	25.0	1.25 (5% of mean)	MPa	Normal	
Azimuth of σ_{Hmax}	060	$\kappa=200$	$^\circ$	Von Mises (circular Normal)	
Fault strike	060	$\kappa=200$	$^\circ$	Von Mises (circular Normal)	
Fault dip	60.0	$\kappa=200$	$^\circ$	Von Mises (circular Normal), truncated at 0 and 90	
Worked Example 2 – Synthetic S_f – modelled depth=3 km					
σ_v , vertical stress	75.0	7.5 (10% of mean)	MPa	Normal	Lithostatic for depth of 3 km, assuming average rock density of 2500 kg m^{-3}
σ_H , max. horizontal stress	55.0	5.5 (10% of mean)	MPa	Normal	
σ_h , min. horizontal stress	35.0	3.5 (10% of mean)	MPa	Normal	

P_f , pore fluid pressure	30.0	3.0 (10% of mean)	MPa	Normal	Hydrostatic for depth of 3 km, assuming fluid density=1000 kg m ⁻³
Azimuth of σ_{Hmax}	060	$\kappa=200$	°	Von Mises (circular Normal)	
Fault strike	060	$\kappa=200$	°	Von Mises (circular Normal)	
Fault dip	60.0	$\kappa=200$	°	Von Mises (circular Normal), truncated at 0 and 90	
Friction, μ	0.6	0.12 (20% of mean)	n/a	Skewed normal	$\alpha = -3$ i.e., skewed low
Cohesion, C_0	20.0	2.0 (10% of mean)	MPa	Skewed normal	$\alpha = +3$ i.e., skewed high

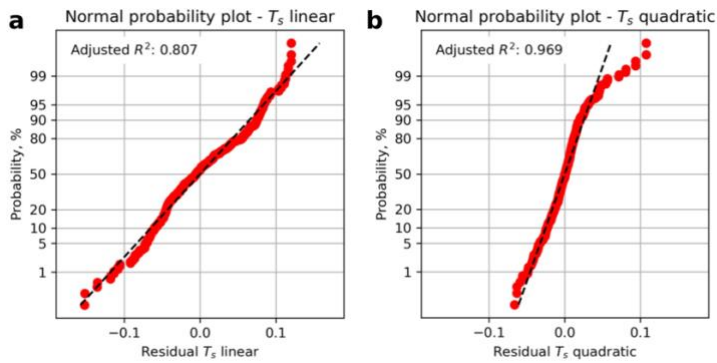
548

549 **Table 2.** Table of input variable distributions for the synthetic models in Worked Examples 1 and 2.



550

551 **Figure 2.** Histograms of input variables used to calculate slip tendency T_s for the synthetic distributions shown
552 in Table 2.



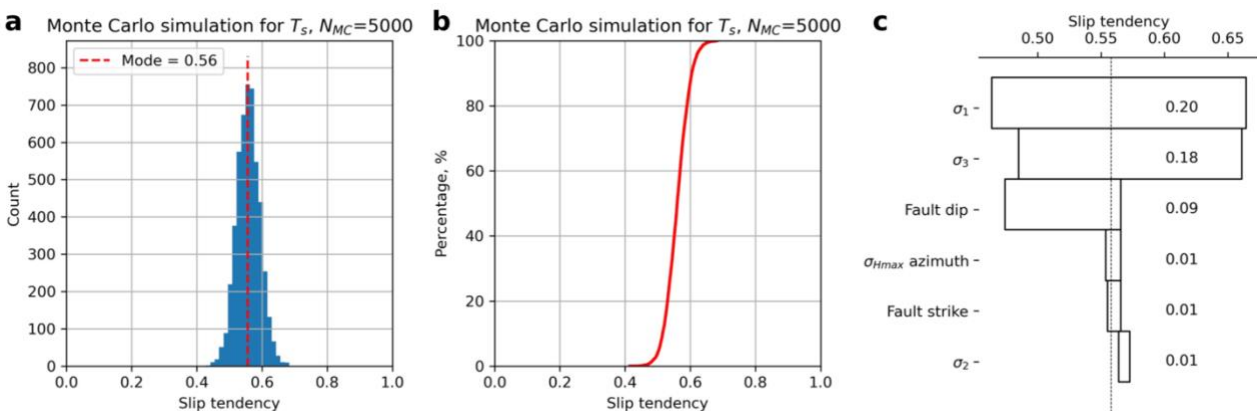
553

554 **Figure 3.** Residual plots for linear and quadratic response surfaces for slip tendency using synthetic data. The
 555 quadratic fit has a higher value of the adjusted R^2 parameter and is therefore deemed better in this case.

556 Having generated the quadratic response surface for T_s for these input distributions, we can now use it to
 557 perform a Monte Carlo (MC) simulation with the aim of generating a statistically viable ensemble from which
 558 we can infer the probability of T_s exceeding a critical value of sliding friction. The results from the MC analysis
 559 of T_s are shown in Figure 4. The histogram of all values of T_s shows a symmetrical and rather narrow
 560 distribution with a modal value of about 0.56 (Figure 4a). The CDF of all values of T_s also shows this narrow
 561 and symmetrical distribution (Figure 4b).

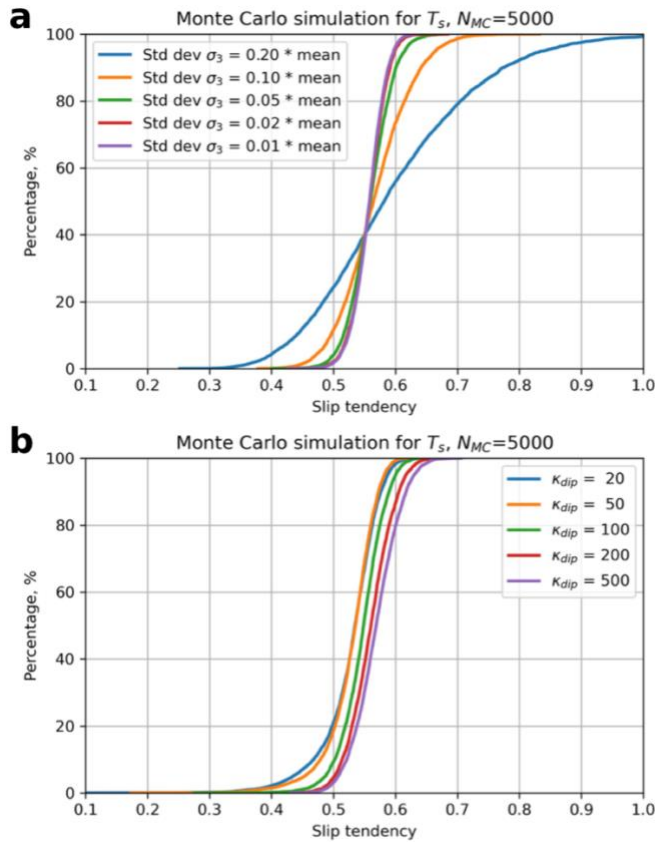
562 A response surface of more than two variables is not easy to visualise. One approach is to take sections
 563 through the surface at specific values of all but one variable and graph that. The red lines shown in Figure 2
 564 depict the response surface for that variable with all other variables held at their mean values. Thus the red
 565 line in Figure 2a shows the variation in T_s as σ_1 varies with all other variables (σ_2 , σ_3 , $sHaz$, φ and δ) held at
 566 their mean values. There is a clear positive correlation of increasing T_s with increasing σ_1 , as expected from
 567 the definition of T_s and its underlying dependence on differential stress ($=\sigma_1 - \sigma_3$); the clear negative
 568 correlation of T_s with σ_3 shown in Figure 2c confirms this. Many of the response surface sections shown in
 569 Figure 2 are quasi-linear, but some are not: in particular, the dependencies of T_s on $sHaz$, strike and dip are
 570 all non-linear, and this further justifies the selection of a 2nd order quadratic response surface model.

571 A useful way to visualise the results from the response surface calculated by the MC simulation is the tornado
 572 plot shown in Figure 4c. Here the ranges of T_s for each input variable (shown as red lines over the histograms
 573 in Figure 2) are plotted to show the relative sensitivity of T_s to each variable. Variables are ranked from the
 574 largest range at the top to the lowest range at the bottom. Again, the core dependence of T_s on differential
 575 stress ($=\sigma_1 - \sigma_3$) is apparent, with σ_1 and σ_3 ranked highest in the plot. Interestingly, fault dip is ranked the
 576 next highest in terms of sensitivity and this reflects the geometry of this particular example. The Andersonian
 577 stress regime is for normal faulting, with σ_1 vertical. σ_2 is oriented parallel to fault strike ($sHaz = strike = 060$),
 578 and the fault dips at 60. This fault is therefore ideally oriented for slip in this stress field. Small changes to dip
 579 will influence the ratio of τ to σ_n , and therefore T_s .



580

581 **Figure 4.** Output from Monte Carlo simulation ($N_{MC}=5,000$) of slip tendency calculated using a quadratic
 582 response surface from synthetic input data. **a.** Histogram of calculated slip tendency values, in this case
 583 showing a quasi-normal distribution with a mode of ~ 0.55 . **b.** Cumulative distribution function (CDF) of
 584 calculated slip tendency values, showing the range in values from ~ 0.4 to ~ 0.7 . **c.** Tornado plot showing
 585 relative sensitivity to the input variables. The vertical dashed line shows the modal (most frequent) value of
 586 T_s from the MC ensemble.



587 **Figure 5.** Output from Monte Carlo sensitivity tests for slip tendency, T_s . **a.** Effect of variation in standard
 588 deviation of the least principal stress, σ_3 . **b.** Effect of variation in dispersion (κ parameter of the Von Mises
 589 distribution) of fault dip.

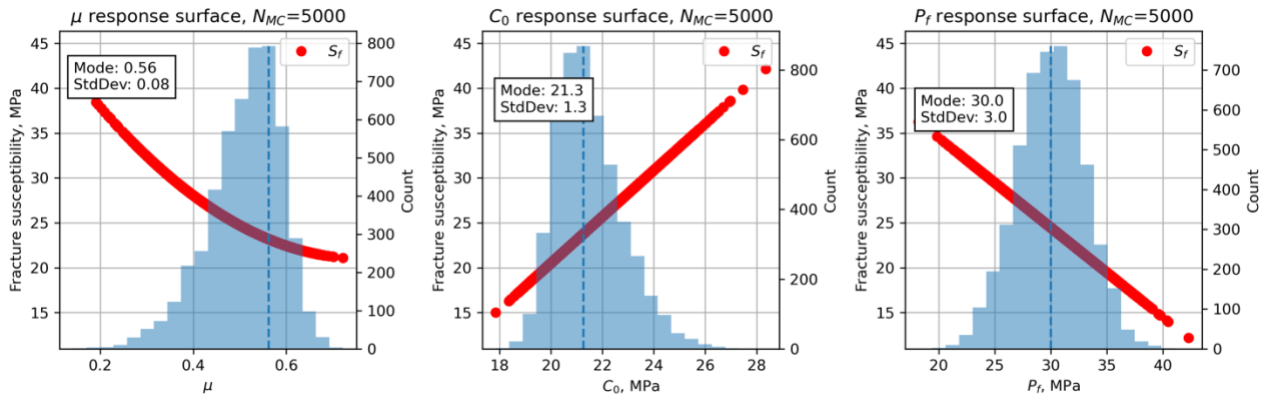
591 We can use a Monte Carlo approach to explore these sensitivities in more detail. Given the shape of the
 592 response surface sections shown in Figure 2 and the ranking of variables in Figure 4c, we can quantify how
 593 more or less variation in the inputs will affect the predicted T_s . Figure 5 shows the results of this sensitivity
 594 analysis for σ_3 and fault dip. The most significant effect on the CDF of T_s is produced by increasing the
 595 variation in σ_3 to 20% of the mean. This level of uncertainty for the minimum stress is not unreasonable in
 596 real-world scenarios (see Case Studies below). Increased uncertainty in σ_3 at this level leads to a $\sim 20\%$ chance
 597 of T_s being in excess of 0.7 ($p = 0.8$ for $T_s \leq 0.7$ from Figure 5a). Increased uncertainty in fault dip is achieved
 598 by varying the dispersion parameter κ of the Von Mises distribution (lower values of $\kappa =$ more dispersed).
 599 Very disperse distributions of fault dip with $\kappa = 20$ only change T_s by < 0.1 .

600 *Worked Example 2: synthetic Sf*

601 We can explore variations in predicted fracture susceptibility using the same principles as for slip tendency,
 602 but adjusted by incorporating three new variables as required by equation 3 – pore fluid pressure, friction
 603 coefficient and cohesion (code in GitHub: WorkedExample2.ipynb). The number of variables q is now 9, and
 604 therefore the design space used to compute the response surface is $3^q = 3^9 = 19,683$ data points. In practice
 605 this means a slower run-time, but still only takes a few minutes on a modern processor.

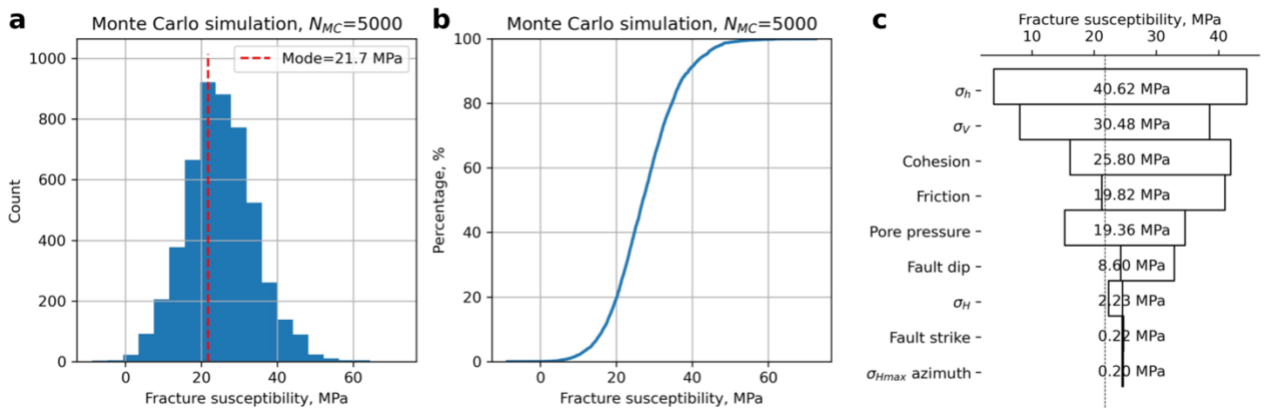
606 For this example, we use the same stress tensor as for the T_s example, with σ_1 as the maximum principal
 607 stress and vertical, i.e., an Andersonian normal fault regime for a depth of approximately 3 km. We constrain

608 the *in situ* pore pressure with a symmetrical normal distribution with a mean value of 30 MPa, which is
 609 approximately hydrostatic for a depth of 3 km, and with a variation of 10% of this mean. Friction is
 610 constrained by a skewed normal distribution with a mode of 0.56 and skewness parameter $\alpha = -3$, i.e.,
 611 skewed towards lower values. This shape of distribution for friction coefficients is consistent with previous
 612 studies (e.g., Moos et al., 2003; Walsh & Zoback, 2016) but is open to question (see Discussion). Similarly for
 613 cohesion, we use a skewed normal distribution with a mode of 21 MPa and $\alpha = +3$, i.e., skewed towards
 614 higher values again consistent with previous work. These input variable distributions are documented in
 615 Table 2 (lower) and shown in the histograms of Figure 6.



616

617 **Figure 6.** Histograms of the input variables, in addition to those shown in Figure 2, used to calculate fracture
 618 susceptibility for the synthetic distributions shown in Table 2. Note the skewed (asymmetric) distributions
 619 for μ and C_0 .

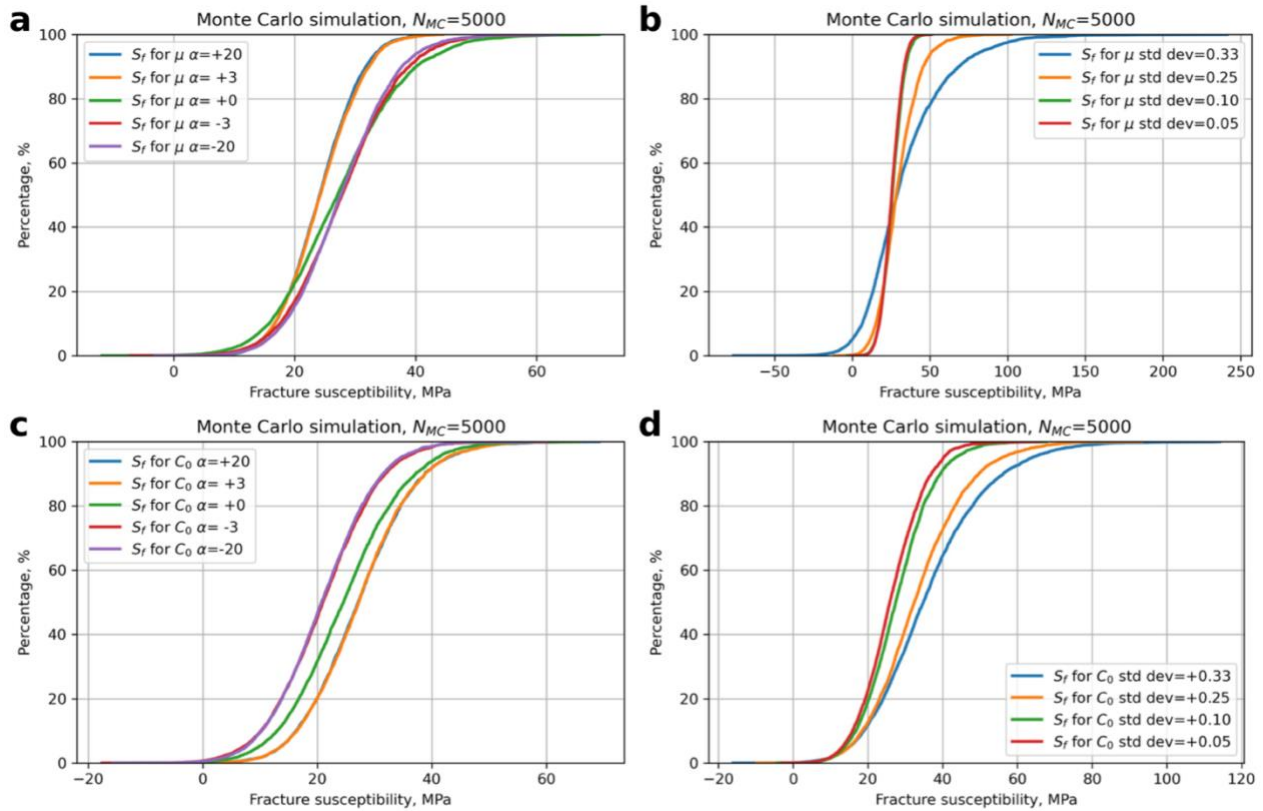


620

621 **Figure 7.** Output from Monte Carlo simulation ($N_{MC}=5,000$) of fracture susceptibility calculated using a
 622 quadratic response surface from synthetic input data. **a.** Histogram of calculated fracture susceptibility,
 623 showing a quasi-normal distribution with a mode of 21.7 MPa. **b.** Cumulative distribution function (CDF) of
 624 calculated fracture susceptibility, showing the range in values from just less than 0 to about 60 MPa. **c.**
 625 Tornado plot of relative sensitivities of the input variables used to calculate fracture susceptibility.

626 We calculate a quadratic response surface and use a Monte Carlo simulation ($N_{MC} = 5,000$) to generate the
 627 ensemble summarised in Figure 7. The mode of the distribution of S_f is 21.7 MPa meaning that, on average,
 628 an increase in pore fluid pressure of about 22 MPa above the average *in situ* value of 30 MPa is needed to
 629 push the effective stress state to Mohr-Coulomb failure. The histogram in Figure 7a is approximately
 630 symmetrical, perhaps with a slight skewness to higher values, and this is reflected in the CDF shown in Figure
 631 7b. The distribution is overwhelmingly positive, meaning that this fault is almost unconditionally stable for
 632 any change in pore fluid pressure, *at these conditions*. The response surface sections for μ , C_0 and P_f shown
 633 in Figure 6 (red lines) all show a strong influence on the fracture susceptibility, and these are confirmed in
 634 the tornado plot of Figure 7c. Pore fluid pressure exhibits a negative correlation with S_f (Figure 6c) which is
 635 consistent with the general principle of effective stress: i.e., if the original *in situ* pore pressure is already

636 high, it only takes a small perturbation (small $\Delta P_f = S_f$) to promote sliding failure. The response to changes in
 637 μ and C_0 is more interesting (Figure 6a and b). For this magnitude of cohesion, the effect of cohesion on S_f
 638 is greater than that of μ (C_0 ranks higher than μ in the tornado plot, Figure 7c), and the dependence of S_f on μ
 639 is negative. However, this relationship is not general as will be shown in the Case Study for the Porthtowan
 640 Fault Zone (see below).



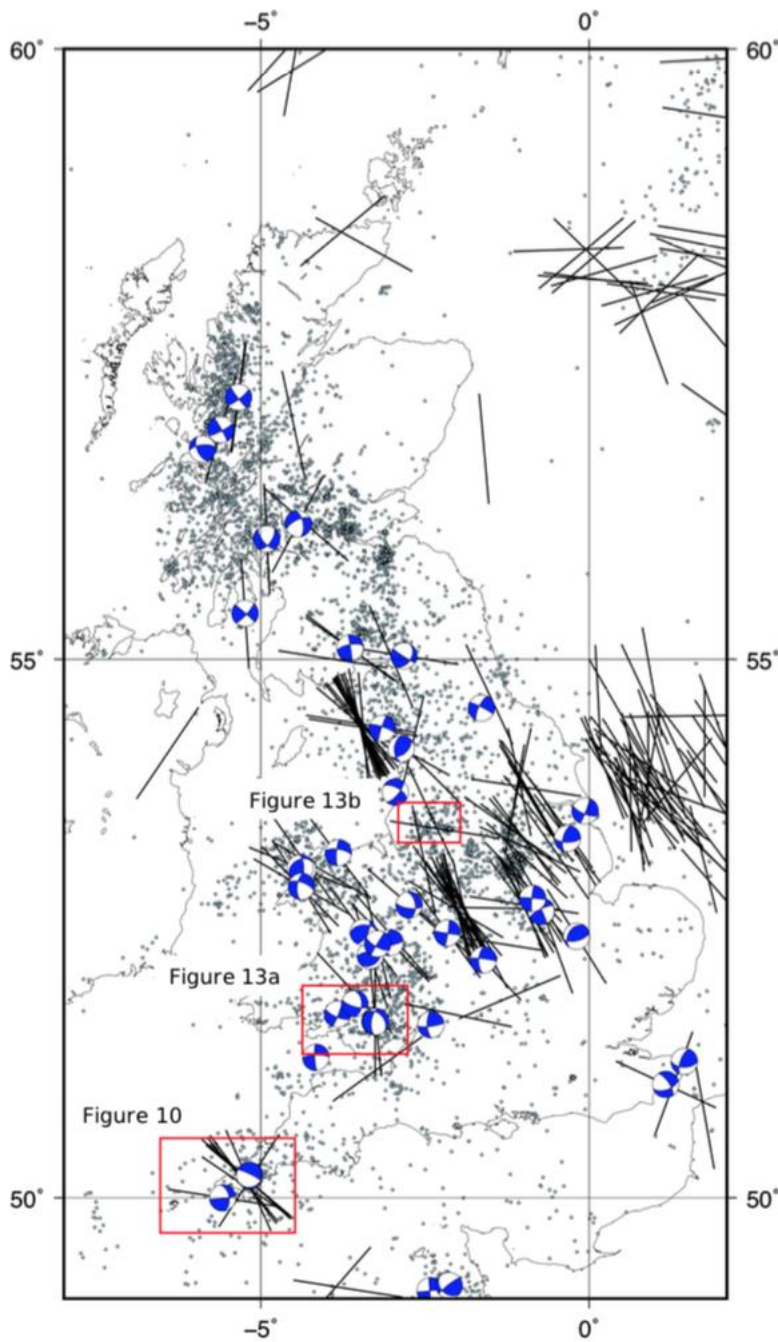
641
 642 **Figure 8.** Sensitivity of fracture susceptibility to variations in μ and C_0 . Note the changes in scale along the x-
 643 axis between the plots.

644 The relative asymmetries of the skewed normal distributions for μ and C_0 have already been noted. Given
 645 their significant effect on S_f (high ranking in the tornado plot, Figure 7c), it is useful to explore how the
 646 skewness of these distributions might influence S_f . Figure 8 shows the results of repeated Monte Carlo
 647 sensitivity tests for μ (Figure 8a, b) and C_0 (Figure 8c, d). For friction, a positive skewness to higher values (α
 648 > 0) would tend to reduce S_f – i.e., faults would be less stable. For cohesion, the opposite is true – a negative
 649 skewness ($\alpha < 0$) would make faults less stable to changes in P_f . These asymmetries are opposite to the ones
 650 used in the main Worked Example 2 and used by other workers (see Discussion). Widening the distributions
 651 for μ or C_0 by increasing their standard deviations (and retaining the original α values) tends to broaden the
 652 distribution of predicted S_f with asymmetry to higher (i.e., more stable) values.

653
 654 **Case Studies**

655 The case studies have been chosen to illustrate how a combined RSM/MC approach can be used to estimate
 656 the probability of slip on one or more faults, and to show that even with relatively good – i.e., complete –
 657 input data, these predictions highlight that industrial operations remain significantly hazardous, with a
 658 greater than 1 in 3 chance of slip on many faults across different settings. Selected specific aspects of the
 659 modelling and the visualisation of results are emphasised in each case study. Figure 9 shows a map of the UK
 660 with the case study areas marked, together with the locations of instrumentally-recorded earthquakes and
 661 their focal mechanisms (Baptie, 2010). Also shown are data from the World Stress Map database of 2016
 662 (Heidbach et al., 2018) indicating the orientation of the maximum horizontal stress. A basic observation from
 663 this map is the level of complexity and heterogeneity in the present day seismotectonics of the UK, reflecting

664 the variation in the subsurface geology. However, there is a broad prevalence of NW-SE trending σ_{Hmax}
665 directions and strike-slip earthquake mechanisms.

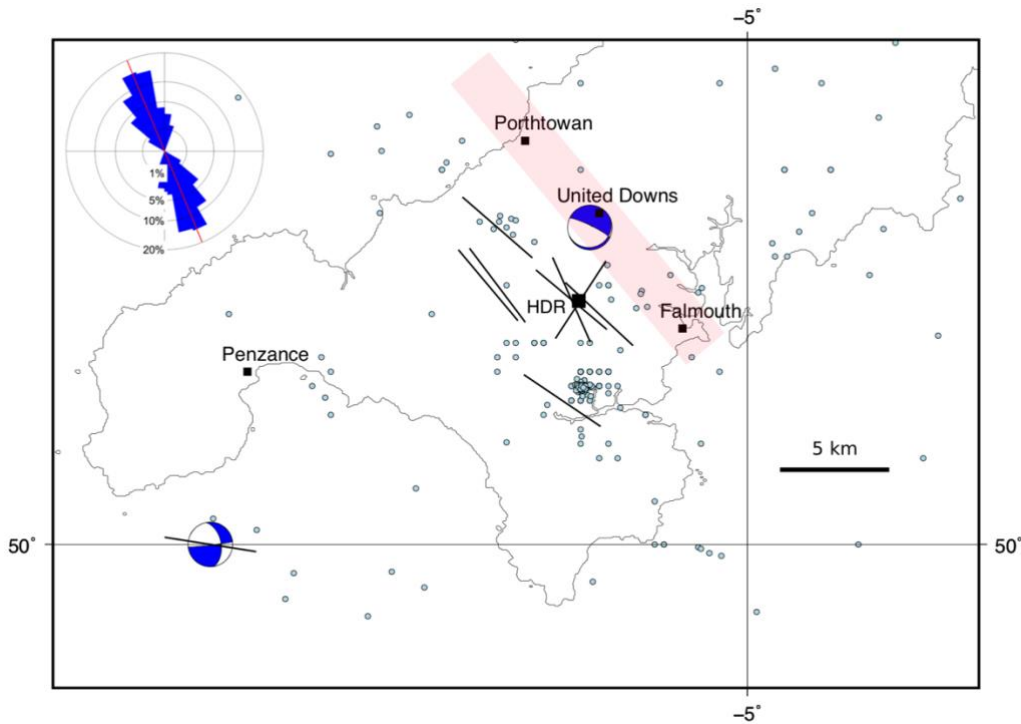


666
667 **Figure 9.** Map of most of the UK showing the locations of the selected case studies. Also shown: epicentres
668 of seismicity (light blue dots; British Geological Survey (BGS) catalogue – Musson, 1996), focal mechanisms
669 (blue and white; Baptie, 2010), and orientations of the maximum horizontal stress (black lines; World Stress
670 Map data – Heidbach et al., 2018).

671 *1. Porthtowan Fault Zone in Cornwall, UK*

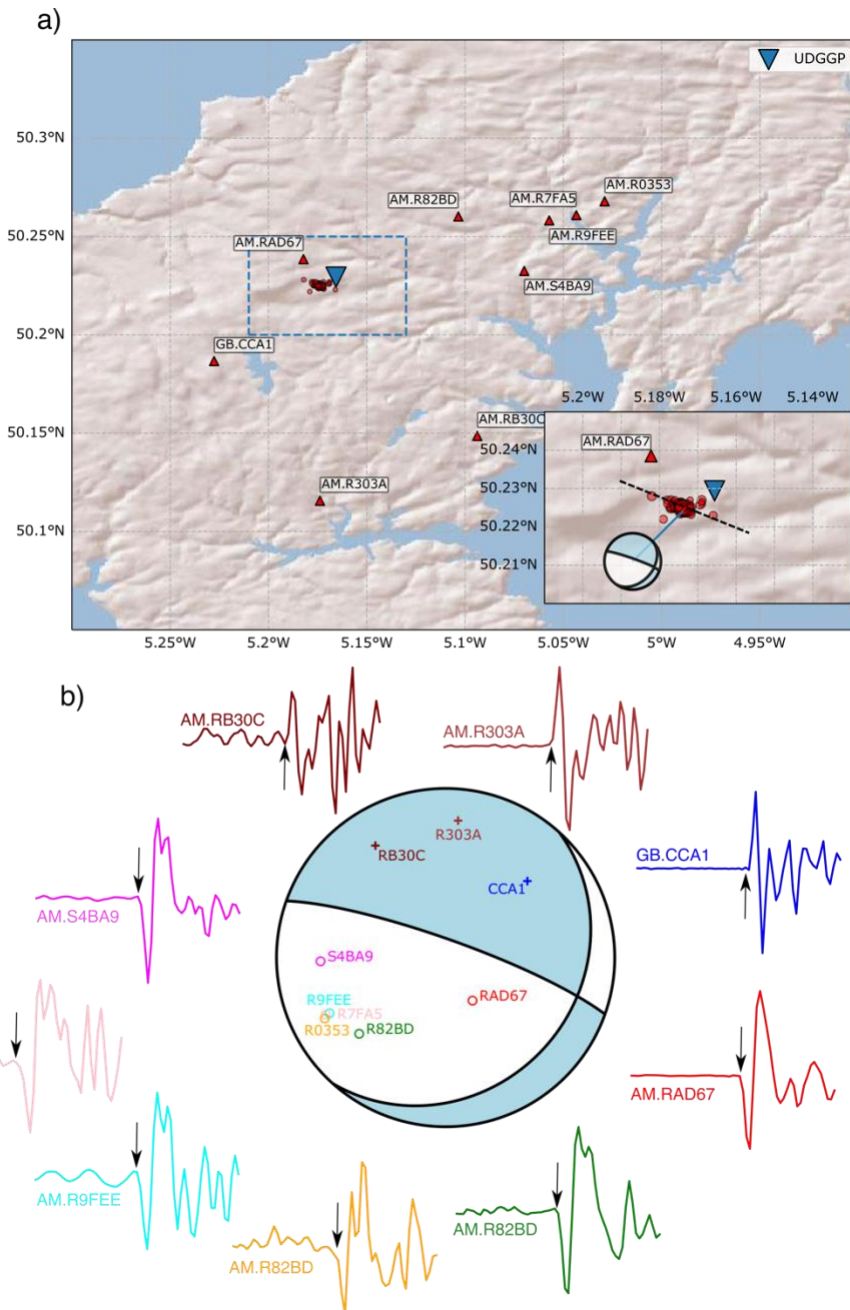
672 The Porthtowan Fault Zone (PFZ) cuts the Carnmenellis granite in Cornwall in southwest England (Figure 10).
673 This granite is a target for deep high-enthalpy geothermal energy due to its high radiogenic heat production
674 (Beamish & Busby, 2016). Following the Hot Dry Rock (HDR) project in the 1980s (Pine & Batchelor, 1984;
675 Batchelor & Pine, 1986), the United Downs pilot project has drilled two boreholes (UD-1, UD-2) to intersect
676 the fault zone at depths of about 5,275 m and 2,393 metres, respectively, making UD-1 the deepest onshore
677 borehole in the UK (Reinecker et al., 2021). The pilot project relies on shear-enhanced stimulation of pre-

678 existing fractures (joints, partially filled veins and faults) to drive fluid flow from the shallow injector (UD-2)
 679 to the deeper producer (UD-1). Temperatures at the base of UD-1 have been predicted at about 200°C
 680 (Ledingham et al., 2019), and recent observations confirm this (Reinecker et al., 2021). Shearing and
 681 downward flow of injected fluid was observed in boreholes as part of the earlier HDR project and tracked
 682 with measured microseismicity (Pine & Batchelor, 1984; Green et al., 1988; Li et al., 2018).



683
 684 **Figure 10.** Map of South West England showing: selected population centres, the United Downs deep
 685 geothermal pilot project and the former Hot Dry Rock project (black squares); epicentres of seismicity (light
 686 blue dots; BGS catalogue – Musson, 1996); focal mechanisms (blue and white; Baptie, 2010); and orientations
 687 of the maximum horizontal stress (black lines; World Stress Map data – Heidbach et al., 2018). Approximate
 688 trend and extent of the Porthtowan Fault Zone shown in pale red. Inset shows an equal area rose diagram
 689 with strikes of fault segments in the Porthtowan Fault Zone measured on BGS Falmouth sheet 352 ($N=140$;
 690 circular mean strike= 158° , circular standard deviation= 27°).

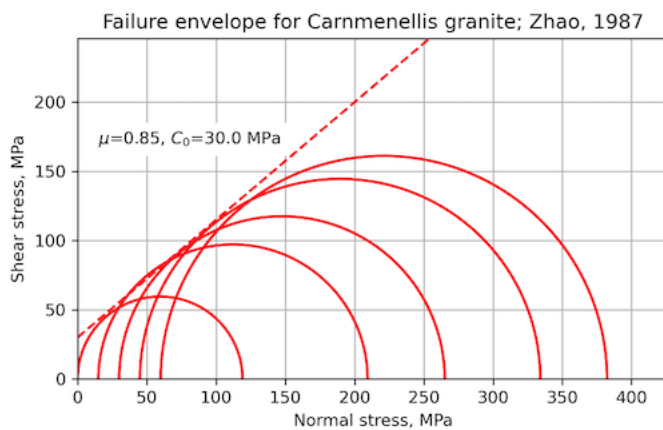
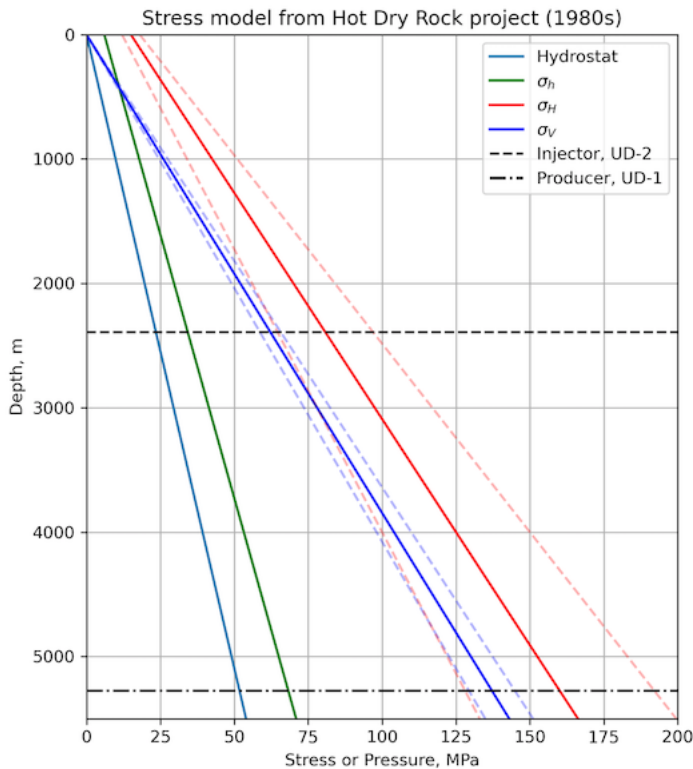
691 Figure 10 shows a map of SW England overlain with seismicity data from the British Geological Survey (BGS;
 692 Musson, 1996). The PFZ is poorly exposed inland, and runs NNW-SSE from Porthtowan on the north Cornish
 693 coast to Falmouth on the south coast (see inset rose diagram for strikes of constituent faults taken from the
 694 BGS Falmouth sheet 352). Overall, the fault zone is believed to dip steeply to the east at around 80° , but note
 695 that there is considerable variation in strike and dip of individual fault and fracture planes within the fault
 696 zone (Fellgett & Haslam, 2021). The azimuth of the maximum horizontal stress is broadly NW-SE, with one
 697 exception trending NE-SW.



698

699 **Figure 11. a.** Red triangles show Raspberry Shake (network code: AM) and BGS (network code: GB) seismic
 700 stations in Cornwall, with station names labelled. Seismicity during geothermal operations is indicated by red
 701 circles. The inset shows a close-up of the area demarcated by the blue dashed line in the main map. The black
 702 dashed line in the inset shows the broad WNW-ESE alignment in seismicity. **b.** Computed focal mechanism
 703 for the 2020-09-30 11:44:01 M_L 1.6 induced earthquake. First-motions are plotted on the focal sphere with
 704 “+” indicating positive polarity, and “o” for negative polarities. P-wave first-motions are plotted starting and
 705 ending 0.3 seconds before and after the picked arrival, respectively, and are coloured in the same way as the
 706 points on the focal sphere.

707



708

709 **Figure 12.** Constraints on input variables for the Porthtowan Fault Zone modelling. **a.** Stress-depth plot based
 710 on data and equations from the Hot Dry Rock project in the Carnmenellis granite (Batchelor & Pine, 1986).
 711 Also shown are the depths of the two wells in the pilot project at United Downs. **b.** Mohr diagram showing
 712 data from laboratory mechanical tests of Zhao (1987) for brittle failure of Carnmenellis granite at 200°C.
 713 Estimated Mohr-Coulomb failure envelope (dashed red line) is defined by $\mu=0.85$, $C_0=30$ MPa.

714 Detailed geomechanical analyses were performed in the Carnmenellis granite in the 1980s as part of the HDR
 715 project, and these provide useful constraints on the variation of stress and fluid pressure with depth (Figure
 716 12a; Batchelor & Pine, 1986). From these data, a strike-slip regime is most likely with $\sigma_1 = \sigma_{Hmax}$ and $\sigma_2 = \sigma_V$,
 717 but note the uncertainties (based on quoted values in Batchelor & Pine, 1986): from around the depth of the
 718 injector well at United Downs and deeper, a normal fault regime is also consistent with the data, i.e., $\sigma_1 = \sigma_V$
 719 and $\sigma_2 = \sigma_{Hmax}$. Note that the earlier HDR project did not target a specific fault zone in the granite.

720 The thermo-mechanical properties of the Carnmenellis granite have been studied by Zhao (1987). Figure 12b
 721 shows a Mohr diagram of data taken from Table 2.3 of Zhao (1987) for laboratory brittle failure tests
 722 conducted at 200°C (the approximate temperature of the injector well at United Downs). From these data,
 723 we have estimated a linear Mohr-Coulomb failure envelope defined by a friction coefficient of 0.85 and a

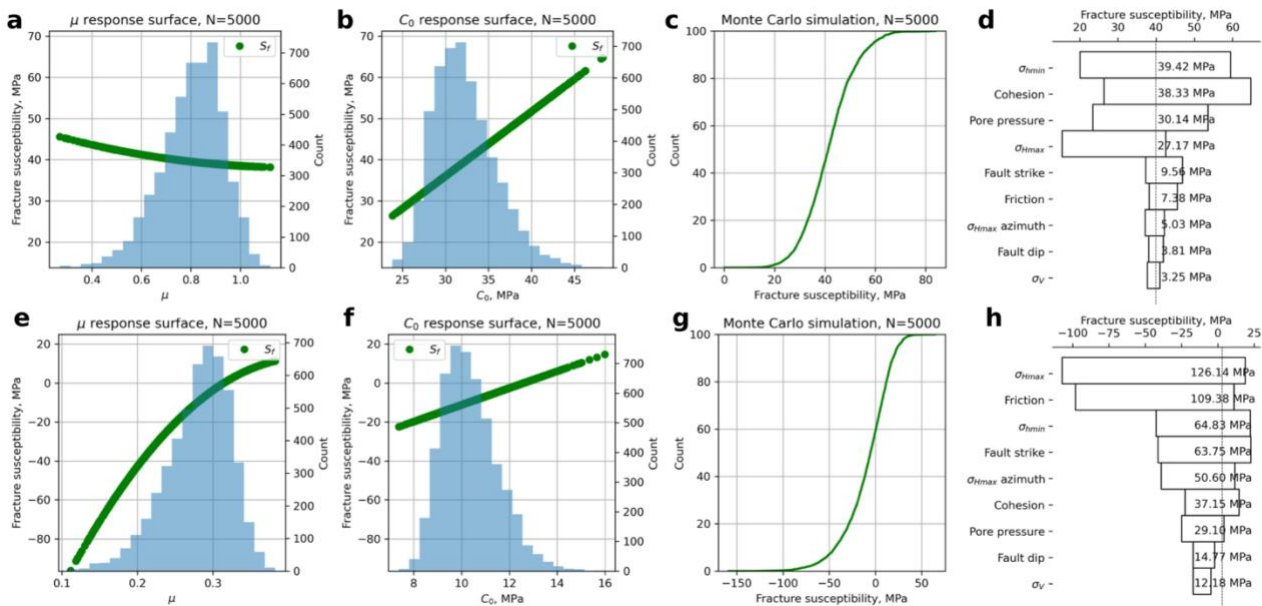
724 cohesive strength of 30 MPa. Cuttings from the boreholes at United Downs have been used to measure
 725 friction coefficients of rocks within the PFZ, and values ranging between $\mu=0.28-0.6$ were recorded (Sanchez
 726 et al., 2020).

727 We present model results for fracture susceptibility in the PFZ as the plan at United Downs (and elsewhere
 728 in the future) is to inject fluid into the fault zone in order to generate shear-enhanced permeability on pre-
 729 existing fractures. Table 3 lists the input variable distributions used in the “base case” model for hydrostatic
 730 pore fluid pressure in the fault zone and mechanical properties taken from laboratory tests of intact
 731 Carnmenellis granite (Figure 12b). The modelled depth is chosen as 4 km, in between the depths of the UD-
 732 1 and UD-2 wells.

Variable	Mean	Standard deviation (κ for Von Mises)	Units	Distribution	Comments
σ_v , vertical stress	105.0	5.25 (5% of mean)	MPa	Normal	Lithostatic for depth of 4 km, assuming average rock density of 2650 kg m ⁻³ Batchelor & Pine, 1986
σ_H , max. horizontal stress	125.0	25.0 (20% of mean)	MPa	Normal	Batchelor & Pine, 1986
σ_h , min. horizontal stress	53.0	5.3 (10% of mean)	MPa	Normal	Batchelor & Pine, 1986
P_f , pore fluid pressure	40.0	4.0 (10% of mean)	MPa	Normal	Hydrostatic for depth of 4 km, assuming average fluid density of 1000 kg m ⁻³
Azimuth of σ_{Hmax}	140	$\kappa=200$	°	Von Mises (circular Normal)	Batchelor & Pine, 1986
Fault strike	340	$\kappa=150$	°	As mapped	Digitised from BGS map
Fault dip	80.0	$\kappa=1000$	°	Von Mises (circular Normal), truncated at 0 and 90	
Friction, μ	0.85	0.17 (20% of mean)	n/a	Skewed normal	$\alpha = -3$ i.e., skewed low
Cohesion, C_0	30.0	6.0 (20% of mean)	MPa	Skewed normal	$\alpha = +3$ i.e., skewed high

733

734 **Table 3.** Distributions of input variables used in the base case model of fracture susceptibility in the
 735 Porthtowan Fault Zone.



736

737 **Figure 13.** Outputs from the Monte Carlo simulation of fracture susceptibility in the Porthtowan Fault Zone.
 738 **a-d.** The response surface for the base case, with friction and cohesion estimated from the laboratory failure
 739 tests of Zhao (1987), predicts positive fracture susceptibility i.e., a stable fault zone. The tornado plot (**d**)
 740 shows that for relatively high values of cohesion (mode of $C_0=30$ MPa in this case), the sensitivity to variations
 741 in friction is slight. **e-h.** In contrast, the response surface for the ‘weak fault’ case, with reduced values of
 742 friction and cohesion (mode of $\mu=0.3$, mode of $C_0=10$ MPa), predicts fault zone instability i.e., overwhelmingly
 743 negative values of S_f . The effect of friction on these predictions is now very strong, as shown in the shape of
 744 the response surface for μ (**e**) and in the ranking within the tornado plot (**h**).

745 The results from the Monte Carlo simulation of S_f for the PFZ are shown in Figure 13. For the base case, with
 746 hydrostatic pore fluid pressure and a ‘strong fault’ (mode of $\mu=0.85$, mode of $C_0=30$ MPa), the fault appears
 747 unconditionally stable for the modelled *in situ* stress variations. The CDF shows almost exclusively positive
 748 values of S_f up to about 60 MPa. Note that, for the input stress variations listed in Table 3, 22% of the MC
 749 simulations produced an Andersonian normal fault regime ($\sigma_1 = \sigma_V$), rather than a strike-slip ($\sigma_2 = \sigma_V$) regime.

750 232 microseismic events with hypocentre depths of 4-5 km were detected by the BGS during geothermal
 751 testing operations in 2021-2022 (http://www.earthquakes.bgs.ac.uk/data/data_archive.html; last accessed
 752 23 July 2021). The largest earthquake induced by geothermal operations during this period occurred on 2020-
 753 09-30 11:44:01, and had a local magnitude of M_L 1.6, and was felt by residents in the area. This event was
 754 well-recorded on a network of single-component Raspberry Shake stations (e.g. Holmgren & Werner, 2021)
 755 and a single station of the BGS permanent monitoring network (Figure 11a). These stations offer excellent
 756 azimuthal coverage of the geothermal seismicity, with the closest station lying only 2 km away (AM.RAD67).
 757 Since no focal mechanisms have yet been documented for these induced earthquakes, we used recorded P-
 758 wave first motions to compute a focal mechanism of the M_L 1.6 event using the method of Hardebeck &
 759 Shearer (2002). Take-off angles were computed using a 1D seismic velocity model for the Cornwall area
 760 (<http://earthwise.bgs.ac.uk/index.php/OR/18/015> Table 4: Depth/crustal velocity models used in eart
 761 [hquake locations](http://earthwise.bgs.ac.uk/index.php/OR/18/015); last accessed 23 July 2021). The best-fitting focal mechanism (Figure 11b) indicates either
 762 normal faulting on a WNW-ESE steeply-dipping plane or strike-slip faulting on a shallow-dipping plane NE-
 763 SW striking plane. Single event relocated epicentres reported by the BGS, which use arrivals from a local
 764 dedicated microseismic monitoring array, show a NW-SE trend (Figure 11a), consistent with normal faulting
 765 on a steeply east-dipping, WNW-ESE striking plane during this earthquake. Negative P-wave polarities were
 766 recorded at AM.RAD67 for all $M > 0$ events, indicating that the same fault plane was reactivated during many
 767 of the induced events. The inferred fault plane is sub-parallel to the interpreted strike of the Porthtowan
 768 Fault Zone that is targeted by the geothermal testing. This observed normal faulting mechanism is consistent
 769 with our MC simulations (more than 1 in 5 of the predicted stress states were for normal faulting).

770

771 The response surface (green lines on Figure 13a-b) and the tornado plot of relative sensitivities of the input
772 variables (Figure 13d) shows a positive dependence of S_f on the cohesion, and that variations in friction are
773 relatively unimportant. If we reduce the strength of the modelled fault zone, by changing the input
774 distributions of μ and C_0 to lower values – but with the same shape and skewness – the situation changes.
775 The predicted fracture susceptibility is now much more strongly correlated with variations in friction, and
776 less so with variations in cohesion. This can be explained by looking at the underlying formula for S_f (equation
777 3), in particular the 2nd term on the RHS. If $C_0 > \tau$ then the numerator of this term can be negative, producing
778 a net positive term. However, if $C_0 < \tau$ and μ is small then this term is larger and negative. The important
779 point is that the probability distribution of S_f (compare Figure 13c and 13g) is controlled by the *relative*
780 magnitudes of μ and C_0 . In a weak fault zone, with low μ and low C_0 , the predictions are very sensitive to the
781 value of friction. In a strong fault, the effect of μ is less important. Thus, we need to know more about the
782 relationship between μ and C_0 in fault rocks (see Discussion).

783 2. South Wales coalfield, UK

784 Scope exists to extract low enthalpy geothermal heat from disused coalmines in the UK (Farr et al., 2016),
785 using either open- or closed-loop technology. Possible sites include the South Wales coalfield, where folded
786 and faulted Coal Measures of Westphalian (upper Carboniferous) age have been mined for centuries, up until
787 the 1980s. Initial plans for shallow mine geothermal schemes include *passive* dewatering which may not
788 change the loading on faults by much. However, *active* dewatering schemes can promote ingress of deeper
789 ground water (Farr et al., 2021), and as this fluid flow must be driven by gradients in fluid pressure, this could
790 in turn lead to the instability of faults at greater depth. The models below are for a depth of 2 km.

791 The locations and orientations of faults have been taken from published BGS maps. We used the BGS
792 Hydrogeology map of S Wales to map the traces of faults in the Coal Measures (Westphalian), and BGS 1:50k
793 solid geology sheets over the same area to collect data on fault dips (Figure 14). Faults were traced onto
794 scanned images of the maps in a graphics package (Affinity Designer on an Apple iPad using an Apple Pencil).
795 These fault trace maps were saved in Scalable Vector Graphics (.SVG) format, after deleting the original
796 scanned image layer of the geological map. The saved .SVG files were read into FracPaQ (Healy et al., 2017)
797 to quantify their orientation distributions (inset rose plots in Figure 14a and b). The fault trace maps were
798 then overlain on maps containing historical seismicity and available focal mechanisms (from the public BGS
799 catalogue; Musson, 1996) and the orientations of σ_{Hmax} taken from the World Stress Map project (Heidbach
800 et al., 2018).

801 In the South Wales coalfield 3,408 fault segments were traced, and the dominant trend is clearly NNW/SSE,
802 but with important (and long) fault zones running ENE-WSW, such as the Neath and Swansea Valley
803 Disturbances (Figure 14). From cross sections, we measured 142 fault dips to help constrain the distribution
804 of friction coefficients in these rocks (Figure 15b-c; see below), corrected for vertical exaggeration on the
805 section line where necessary. Focal mechanisms in this area ($n=4$) suggest that NNW/SSE and N/S faults are
806 active in the current stress regime. Historical seismicity is widely, if unevenly, distributed with no obvious
807 direct correlation to the surface mapped fault traces. For example, there are areas of intense surface faulting
808 but no recorded historical seismicity, and vice versa – areas with abundant historical events but few mapped
809 faults.

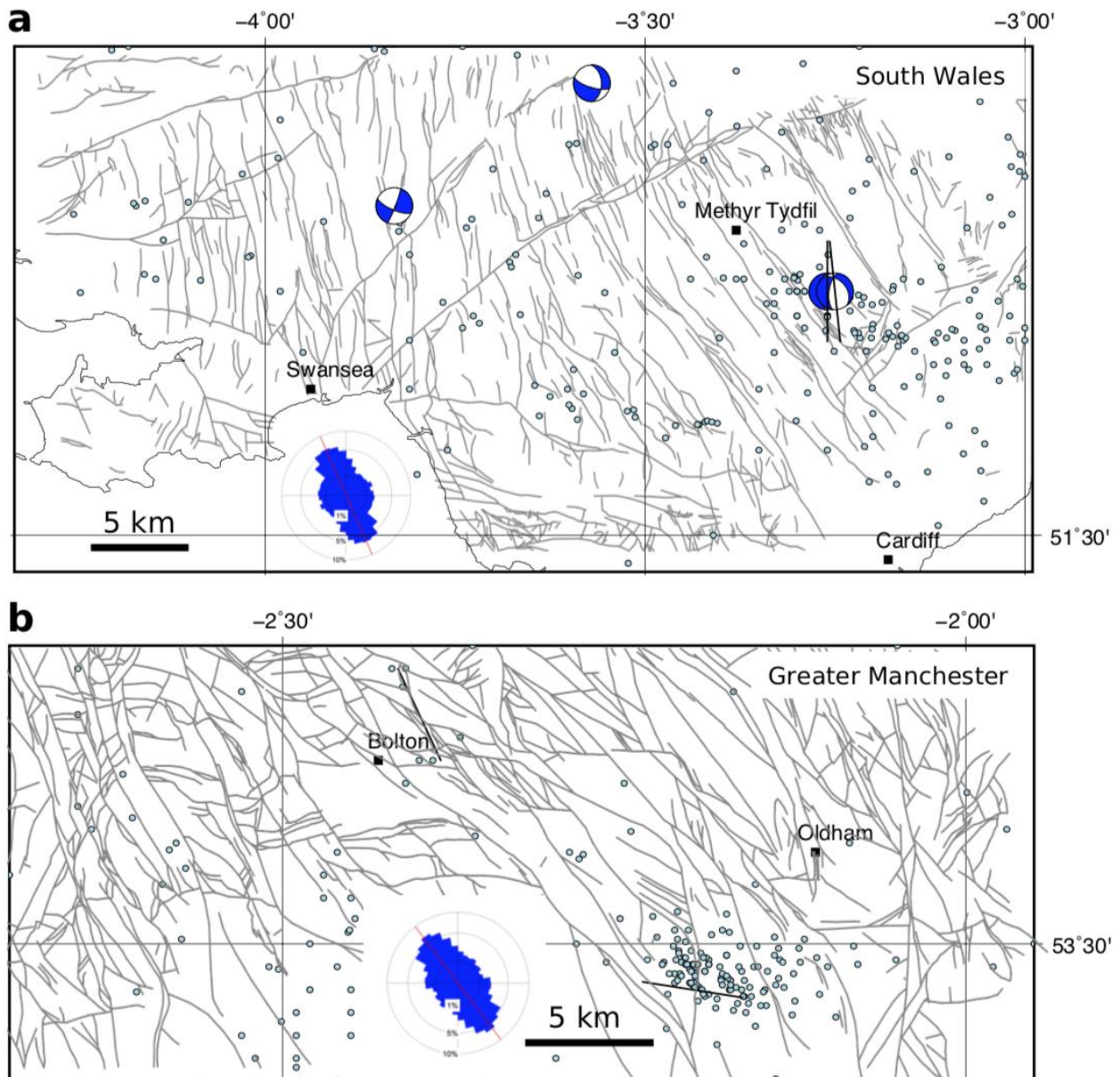
810 There are no published geomechanical analyses for the variation of stress with depth for this area. To
811 constrain the depth dependence of stress, we have used larger scale syntheses of stress for onshore UK
812 produced by the BGS (e.g., Kingdon et al., 2016; Fellgett et al., 2018). The stress-depth plot in Figure 15a has
813 been constructed using the data shown in Fellgett et al. (2018), and shows that, in general, a strike-slip fault
814 regime with $\sigma_1 = \sigma_{Hmax}$ is most likely. However, given the known uncertainties in these data, a normal fault
815 regime ($\sigma_1 = \sigma_v$) cannot be ruled out, especially at depth. Note that the stress-depth data shown in Fellgett
816 et al. (2018) and used in Figure 15a are compiled from different areas, and remain untested for the specific
817 area shown in this paper. The azimuth of σ_{Hmax} is known to vary across the UK ranging from ~130 to ~170
818 (Baptie et al., 2010; Becker & Davenport, 2001).

819 Despite the economic and historical significance of the Coal Measures, there are no published datasets of
820 laboratory measured friction or cohesion for either intact rocks or their faulted equivalents (although data

821 may exist in proprietary company records). Data for specific units of interest does exist, e.g., for the
822 Oughtibridge Ganister, a seat earth in the Coal Measures (Rutter & Hadizadeh, 1991); and the Pennant
823 Sandstone, a rare marine sandstone unit (Cuss et al., 2003; Hackston & Rutter, 2016), but a systematic
824 analysis of the volumetrically dominant sandstone, siltstone and mudstone formations is notably absent.
825 Instead, we use the measured dips of faults in the Coal Measures as a proxy for the coefficient of sliding
826 friction, using the relationship

827
$$\mu = 1/\tan(\pi - 2\beta)$$
 equation 14

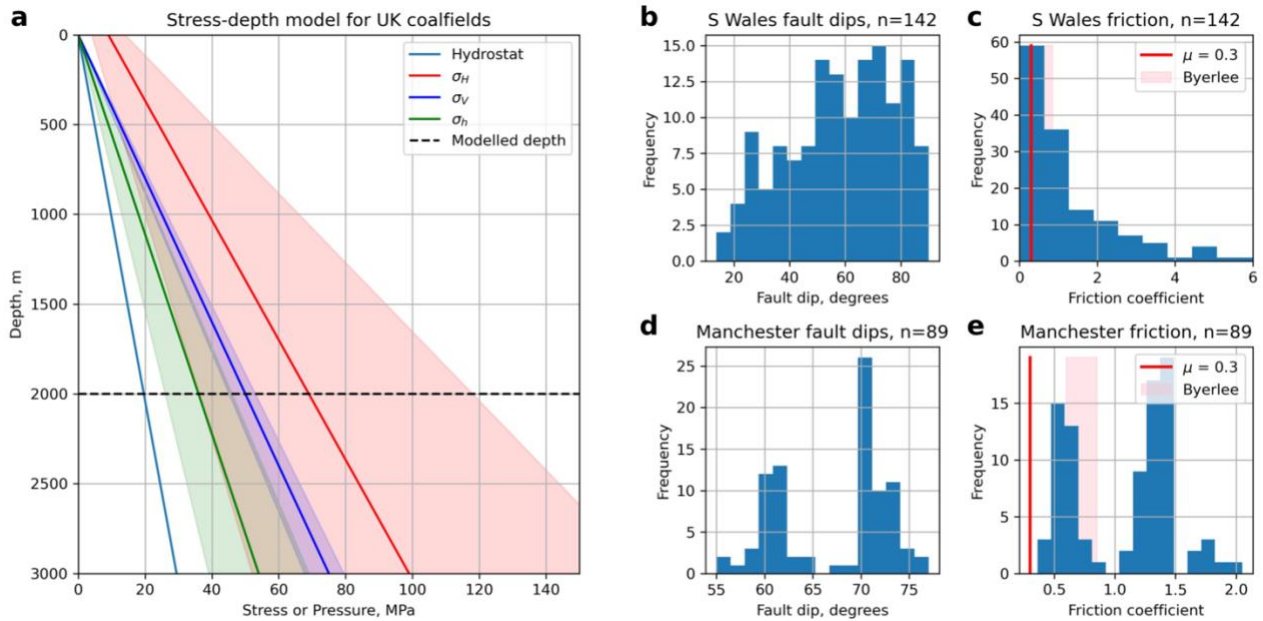
828 where β is the angle between the fault plane and σ_1 at failure (Jaeger et al., 2009; Carvell et al., 2014). Such
829 a calculation assumes Mohr-Coulomb failure and that the current dip of the fault is reasonably close to the
830 dip at failure in the post-Westphalian deformation of the coalfields. For measured fault dips $< 45^\circ$, we assume
831 that σ_1 was horizontal (Andersonian thrust/reverse fault regime) and for fault dips $\geq 45^\circ$ we assume σ_1 was
832 vertical (Andersonian normal fault regime). In practice, some of these faults probably originated as strike-slip
833 faults (i.e., with a sub-vertical dip and σ_2 vertical), and some of their dips have almost certainly been modified
834 by compaction since their formation. However, this method of estimating the likely range of friction
835 coefficients from measured dips remains simple to apply and useful to first order, in the absence of better
836 data. From the dip data, the calculated friction coefficients vary between 0.0 and 6.0 for South Wales (Figures
837 15b, c).



838

839 **Figure 14.** Maps of South Wales coalfield (a suggested site of shallow mine geothermal energy) showing:
 840 selected population centres (black squares); epicentres of seismicity (light blue dots; BGS catalogue –
 841 Musson, 1996); focal mechanisms (blue and white; Baptie, 2010); and orientations of the maximum
 842 horizontal stress (black lines; World Stress Map data – Heidbach et al., 2018). Inset equal area rose diagrams
 843 show orientations of mapped faults. Faults in the Coal Measures taken from the BGS Hydrogeological Map
 844 of South Wales (1:125k) ($n=3,408$), with a circular mean strike= 156° and a circular standard deviation= 65° .

845 Based on the values of sliding friction calculated from measured fault dips across both coalfields a threshold
 846 stability value of $\mu=0.3$ is taken as a reasonable lower bound for faulted rock. This is the value used to
 847 compare with predicted slip tendencies calculated for each fault. For $T_s > 0.3$, the fault is deemed unstable,
 848 for $T_s \leq 0.3$ it is stable.



849

850 **Figure 15.** Constraints on input variables for the coalfield modelling of slip tendency. **a.** Stress-depth plot
 851 based on data from onshore UK (after Fellgett et al., 2018). Also shown is the modelled depth of 2 km. **b-c.**
 852 Histograms of fault dips measured cross-sections on published BGS 1:50k maps of South Wales, and
 853 calculated values of friction coefficients derived from these dips assuming Mohr-Coulomb failure. Byerlee
 854 friction ($\mu=0.6-0.85$) shown as shaded pink box. Modelled critical values of friction ($\mu=0.3$) shown by red lines.

855

Variable	Mean	Standard deviation (κ for Von Mises)	Units	Distribution	Comments
South Wales coalfield T_s model, depth=2 km					
σ_v , vertical stress	50.0	3.75 (5% of mean)	MPa	Normal	Lithostatic for depth of 2 km, assuming average rock density of 2500 kg m^{-3}
σ_H , max. horizontal stress	70.0	14.0 (20% of mean)	MPa	Normal	After Fellgett et al., 2018
σ_h , min. horizontal stress	35.0	3.5 (10% of mean)	MPa	Normal	After Fellgett et al., 2018
Azimuth of σ_{Hmax}	160	$\kappa=200$	$^\circ$	Von Mises (circular Normal)	After Fellgett et al., 2018; Baptie, 2010; WSM, 2016
Fault strike	-	-	$^\circ$	As mapped	Digitised from BGS Hydrogeology sheet
Fault dip	n/a	$\kappa=25$	$^\circ$	Von Mises (circular Normal), truncated at 0 and 90	Fitted to data taken from cross-sections on BGS 1:50k sheets 229-231, 247-249, 263, 263

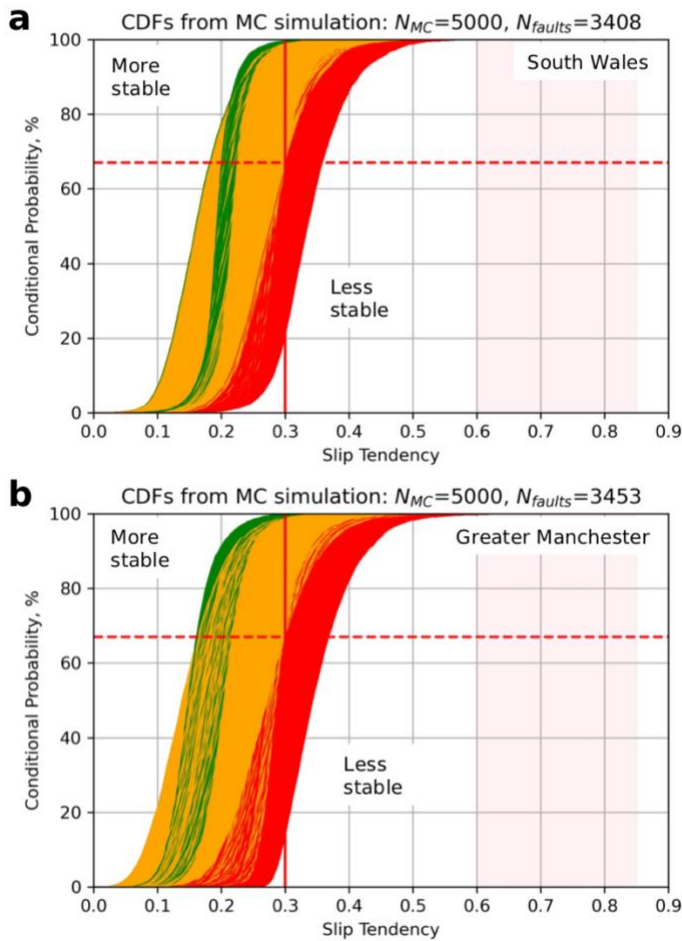
856

857 **Table 4.** Distributions of input variables used to model slip tendency in the coalfield of South Wales.

858 Predictions of conditional probability for fault slip have been calculated for all faults in the coalfield using slip
 859 tendency as the chosen measure: in the absence of detailed pore fluid pressure constraints or estimates of
 860 cohesive strength, it is hard to justify modelling the fracture susceptibility. Slip tendency provides a first order

861 estimate of fault stability. A quadratic response surface was constructed for the coalfield using the full range
 862 of measured fault strikes and dips, and the input variable distributions listed in Table 4 and constrained by
 863 the data in Figure 15. Monte Carlo simulations ($N_{MC}=5,000$) were run for each mapped fault segment with
 864 the other input variables drawn from their respective distributions.

865 Output CDFs for all faults are shown in Figure 16. For South Wales ($N=3,408$ faults), approximately 46% of
 866 faults are predicted to have a 1 in 3 chance of being unstable (i.e., $T_s > 0.3$, shown in red), and 42% of faults
 867 are predicted to have a 1 in 10 chance of being unstable (shown in amber).



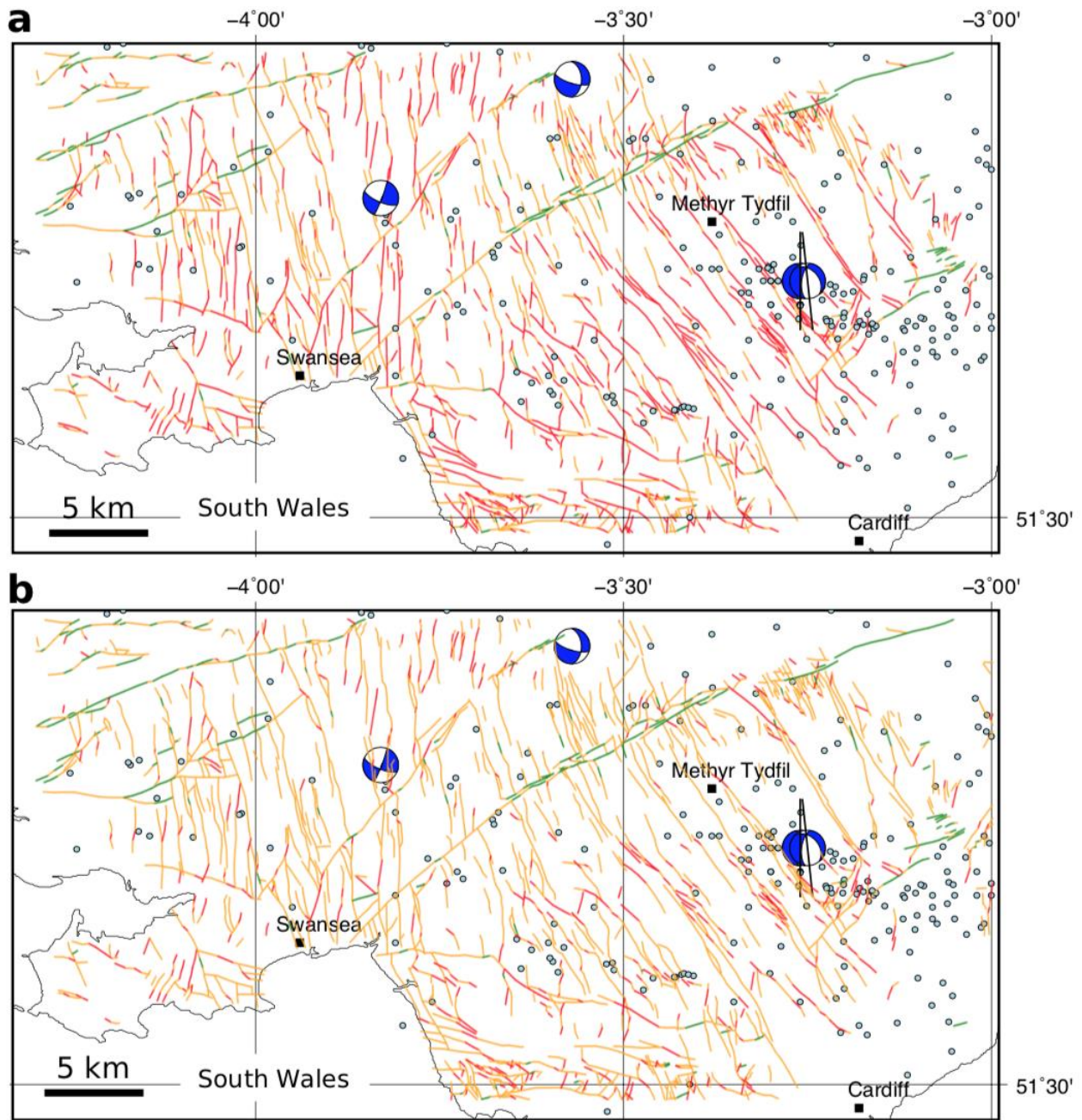
868

869 **Figure 16.** Output from the Monte Carlo modelling of slip tendency in South Wales coalfield, UK. For slip
 870 tendency, more stable faults skew towards the left (low T_s), less stable faults skew to the right (high T_s). CDFs
 871 of predicted slip tendency for each mapped fault in South Wales. Colour coding of CDFs – red: >33% chance
 872 of exceeding threshold friction ($\mu=0.3$, vertical red line), amber: >1% and <33% chance, green: < 1% chance.
 873 Range of Byerlee friction shown by pink shading.

874 The results from the RSM/MC modelling shown in the CDFs are replicated in map view in Figure 17. Each
 875 fault segment is colour coded using the same heuristic applied in the CDF: red faults have a conditional
 876 probability of at least 33% of their slip tendency exceeding the chosen threshold value of fault rock friction
 877 ($\mu=0.3$), amber (orange) faults have a 1-33% chance, and green faults have a less than 1% chance of being
 878 unstable.

879 For South Wales, the general pattern of the predictions is consistent with the recorded focal mechanisms
 880 (Figure 17a). The most likely fault segments to slip (coloured red) are those oriented either NNW/SSE or N/S,
 881 corresponding with one of the nodal planes in each of the focal mechanisms. Faults trending ENE/WSW, such
 882 as the Neath Disturbance, are predicted to have low probability of slip in the modelled stress regime (green).
 883 Note that the Swansea Valley Disturbance trends ENE/WSW as a fault zone, but the constituent fault
 884 segments are variously oriented including elements that trend NE/SW, and these are marked in red (high
 885 probability of slip). Blenkinsop et al. (1986) noted that this fault zone may in fact have a shallow dip at depth,

886 which is not covered by the dip distribution used in our modelling, so further work is required here. The
 887 location with the most recorded events lies to the SE of Merthyr Tydfil, and this corresponds to an area with
 888 many mapped faults trending NW/SE marked with a high probability of slip, and consistent with two of the
 889 focal mechanisms.



890
 891 **Figure 17.** Output from the Monte Carlo modelling of slip tendency in South Wales coalfield. **a.** Colour-coded
 892 fault map showing conditional probability of slip for each mapped fault. This map shows the unweighted
 893 values, as shown on the CDFs in Figure 14a. **b.** Colour-coded fault map showing conditional *weighted*
 894 probability of slip for each mapped fault. The weighted probability is calculated by multiplying the probability
 895 from the CDF in Figure 14a by the normalised fault smoothness, ranging from 1.0 for a perfectly straight (i.e.,
 896 smooth) fault, and tending to 0.0 for a rough fault. Colour coding of CDFs – red: >33% chance of exceeding
 897 threshold friction ($\mu=0.3$), amber: >1% and <33% chance, green: < 1% chance.

898
 899

900 Discussion

901 *Stress, pressure, and temperature*

902 The simulations described in this paper all critically depend on our knowledge of the *in situ* stress tensor. We
903 can constrain some of the components of this tensor better than others. The vertical stress (σ_v) is usually the
904 best constrained, a reflection of its derivation from the borehole density logs sampled at sub-metre
905 resolution. Our estimates of the horizontal stresses, σ_{Hmax} and σ_{Hmin} , remain poorly constrained. Even in cases
906 with relatively good data, e.g., from borehole leak-off tests (LOTs) and formation integrity tests (FITs), the
907 “data density” for these stress components is generally sparse (compared to σ_v), and we are stuck with
908 significant uncertainties. And these uncertainties matter, as shown by this study and previous work (e.g.,
909 Chiaramonte et al., 2008; Walsh & Zoback, 2016). The fundamental dependence of shear failure on
910 differential stress inherent in the Mohr-Coulomb failure criterion is reflected in the high ranking of stress
911 tensor components in the tornado plots shown in this study. Also, larger uncertainties in stress components
912 mean that the Andersonian regime may flip from the default “average” assumption to another orientation:
913 e.g., an apparently strike-slip regime may in fact include a significant proportion of normal fault possibilities
914 (>20% in the case of the Porthtowan Fault Zone shown here). One way to improve our knowledge of the
915 stress tensor, and especially the azimuth of σ_{Hmax} would be to exploit richer catalogues of seismicity to
916 produce more focal mechanisms for natural or induced events. Most countries would benefit from better –
917 i.e., more widespread and higher resolution – continuous seismic monitoring. While this may be expensive
918 with top of the range broadband equipment, citizen science devices, such as the Raspberry Shake, offer a
919 low cost and viable alternative (Cochran, 2018; Anthony et al., 2019; Hicks et al., 2021; Holmgren & Werner,
920 2021). Our study shows how Raspberry Shake data are effective for computing focal mechanisms. Analysis
921 of more events would allow stress inversions to be performed on the data measured by these devices,
922 especially when they are combined in *ad hoc* arrays to improve signal to noise ratios.

923 Pore fluid pressures at depth are also poorly known, even for a country like the UK with a long tradition of
924 geological (and geophysical) science and rich history of mining and drilling into the crust. Most importantly,
925 our knowledge of measured *in situ* pore fluid pressures in and around fault zones is generally poor.
926 Theoretical predictions and model simulations abound, but direct measurements of this key parameter are
927 almost non-existent. We need to know the actual limits of pore fluid pressures in fault zones, and their likely
928 spatial and temporal variation over a fault plane throughout the seismic cycle. The situation is complicated
929 by the finer scale structure of fault zones. Fault zones in low porosity and/or crystalline rocks (such as granite)
930 can be divided into one or more narrow cores defined by fine grained fault rocks (gouges, cataclasites)
931 surrounded by wider damage zones of more or less fractured rock. Permeability may be low in and across
932 the core(s) and higher in the damage zones (Caine et al., 1996; Faulkner et al., 2010). In high porosity and/or
933 granular rocks (such as sandstone), fault zones may be simpler, with a fine grained fault rocks along narrow
934 fault planes forming an effective fluid seal (Wibberley et al., 2008) These differences in the physical
935 characteristics of the fault zones have consequences for the distribution of dynamic pore fluid pressures,
936 which remain poorly known in detail.

937 The work described in this paper has ignored the effects of temperature. However, thermoelastic stress may
938 be more important than poroelastic stress by a factor of 10 (Jacquey et al., 2015). In short, colder injected
939 water may increase the chance of slip on a given fault. In the UK, our knowledge of the subsurface
940 temperature field is increasing (Beamish & Busby, 2016; Farr et al., 2021), but we need more data, and again,
941 especially from faulted rocks.

942 *Faults*

943 An implicit assumption in all of the modelling performed in this paper (and many others) is that we know
944 something about the fault which may slip: i.e., we can only quantify risk on known faults. There will, in
945 general, be many more unmapped faults in the subsurface, and these may be the ones most likely to slip due
946 to a change in loading (of either *in situ* stress or fluid pressure). This is apparent in the maps for the coalfields
947 shown in this paper in terms of the relative lack of correspondence between the surface mapped fault traces
948 and the locations of recorded earthquakes. Some of this “mismatch” could be explained by the dip of the
949 faults measured at the surface, but not all. Moreover, there are areas of apparently intense surface faulting

950 and no recorded seismicity, and vice versa (recorded seismicity but no mapped surface faults). Some advance
951 could be made to address this problem with the recognition that each recorded seismic event documents a
952 fault plane, assuming that a double couple focal mechanism implies fault slip rather than dilation from dyke
953 emplacement or other mechanisms. And therefore the 3D position of each focal mechanism points to at least
954 part of a subsurface fault. The challenge then lies in mapping these seismic event fault planes into a viable
955 fault network. Better data (i.e., higher spatial resolution and extending to smaller event magnitudes) from
956 more dense arrays of seismometers would help with this task, as for the refinement of stress estimates noted
957 above.

958 *Rock properties*

959 The importance of good data on rock properties has been emphasised above, in the Worked Example for
960 fracture susceptibility and in the case study for the Porthtowan Fault Zone. In general, we need more and
961 better data on coefficients of friction and cohesive strength, especially for the target formations of
962 decarbonisation operations. Moreover, we need data for the intact *and* faulted rocks. We also need better
963 constrained correlations among rock properties. A widely used method in oil and gas is to derive estimates
964 of friction coefficient and UCS from wireline log datasets measuring porosity, slowness (velocity) or elasticity
965 e.g., Chang et al., 2006. However, as noted by these authors, the correlations are strictly valid only for the
966 specific formations tested in the laboratory, and even then, the uncertainties remain large. A further issue is
967 the tendency to average wireline log derived estimates over a depth interval, when for most sections of crust
968 this is the direction in which rock properties are expected to vary most rapidly. The Porthtowan Fault Zone
969 example above highlighted another issue: the relative impact of cohesion and friction on the predicted
970 stability depends on the magnitude of the cohesion in relation to the shear stress on the fault. For low
971 cohesion values, the constraints on friction become much more important. We need systematic
972 investigations of frictional behaviour at low cohesive strength. We need detailed systematic correlations
973 among rock properties, especially for faulted crystalline basement rocks.

974 Collecting more laboratory data is no panacea, evidenced by the well-aired concerns over how we up-scale
975 rock properties and behaviours from mm- and cm-sized samples to whole fault zones. But calibrations and
976 correlations from careful, systematic laboratory data remain the cornerstone of estimating the key *in situ*
977 values. An interesting new focus would be to explore the nature of the skewness in mechanical property
978 datasets: why should friction coefficients skew low, and cohesive strength skew high?

979 The utility of the Mohr-Coulomb criterion used in this paper is largely down to its mathematical simplicity,
980 i.e., linearity and only two parameters (friction and cohesion). Other criteria are perfectly viable and could
981 easily be added to the pfs Python code, but some other failure criteria lack a clear mapping between their
982 parameters and the mechanics of sliding on rock surfaces.

983 *Applicability of T_s , T_d and S_f for quantifying risk*

984 A valid question is to ask whether any of these widely used measures of fault stability are, in fact, useful in
985 practical terms at the scale of faults on maps. All three measures focus on the simplified mechanics of slip on
986 a specific fault plane, with a fixed orientation and with specific rock properties. But seismic hazard is not
987 isolated at the level of single fault planes. Faults occur in patterns or networks, more or less linked together.
988 Geometrical factors may be more important than the specifics of either the *in situ* stress or the rock
989 properties, at the scale of observation. The observational record shows that bigger fault zones are the sites
990 of bigger earthquakes, and they are also the locus of most displacement in a given network. Conversely,
991 smaller faults host smaller seismic events, and accrue less overall displacement (Walsh et al., 2001). To begin
992 to address this issue, we can weight the conditional probabilities of slip for a specific fault segment by a
993 dimensionless normalised factor derived from the total length of the fault: e.g., $w_{size} = l_s / l_t$ where l_s is fault
994 segment length and l_t is fault trace length. An alternative, but related idea, is that of the relationship between
995 fault smoothness (or inversely, roughness) and fault maturity, and therefore seismic hazard (Wesnousky et
996 al., 1988; Wells & Coppersmith, 1994; Leonard, 2010). The most seismically active faults are not only, or
997 necessarily, the largest ones in their network, but tend to be the smoothest or most connected, reflecting
998 the coalescence of fault segments through time and the removal of asperities through repeated slip events
999 (Stirling et al., 1996). Therefore, we can weight the conditional probabilities of slip by a dimensionless factor

1000 of smoothness: $w_{smooth} = l_{straight} / \text{sum}(l_s)$, where $l_{straight}$ is the straight line length between fault end points,
1001 which is 1.0 for a perfectly smooth fault with all segments parallel and connected, and tends to 0.0 for rough,
1002 complex fault traces. Examples of the effect of these smoothness weightings applied to the conditional
1003 probabilities are shown in Figure 17b for the South Wales coalfield faults. The net effect is to reduce the
1004 number of most risky faults (shown in red) by about half. These approaches are the subject of further work
1005 and testing.

1006

1007 Summary

1008 In this paper, we have described and explained the Response Surface Methodology and shown how it can be
1009 combined with a Monte Carlo approach to generate probabilistic estimates of fault stability using published
1010 measures of slip tendency, dilation tendency and fracture susceptibility. Simulations show that a quadratic
1011 response surface always generates a better fit to the input variables in comparison to a linear surface, at the
1012 cost of larger matrices (more computer memory) and longer run times. Worked examples to calculate T_s and
1013 S_f with synthetic input distributions show how the quadratic response surfaces vary for each input parameter.
1014 For slip and dilation tendency, the primary dependence is (as expected) on the maximum differential stress,
1015 and therefore the maximum and minimum principal stresses of the *in situ* stress tensor, with a lesser
1016 dependence on the fault orientation. For fracture susceptibility, the situation is more complex: if cohesion is
1017 relatively high, S_f is mainly dependent on the *in situ* stresses and cohesion. But if cohesion is low – quite likely
1018 in fault zones – then the dependence of S_f on friction is much more significant. This is a key finding: the
1019 relative sensitivity of the input variables on the response surface varies with the absolute value of the
1020 variables.

1021 Sensitivity tests were used to assess how the shapes of different input distributions affect the predictions of
1022 fault stability. Varying the spread of symmetric (normal, Gaussian) distributions of input variables has a
1023 significant effect on the predictions, and this mirrors the reality of uncertainties in, for example, the principal
1024 stresses in a standard geomechanical analysis. As noted above, the vertical stress is often well constrained
1025 and has a lower relative standard deviation (say, 5% of the mean) than either the maximum or minimum
1026 horizontal stresses (typically 15-20% of their mean value). The shape and spread of skewed (asymmetric)
1027 distributions of rock properties (friction and cohesion) is also important. The direction of skewness is
1028 described by the sign of the parameter α for the skewed normal distributions used in this paper to model
1029 variations in rock properties. Friction is modelled with a negative skewness towards lower values, whereas
1030 cohesion is modelled with positive skewness towards higher values, but systematic laboratory data are
1031 needed to verify these assumptions. This will require a statistically significant number of repeat tests for each
1032 property on quasi-identical samples of the same rock.

1033 Case studies of three different locations demonstrated how a probabilistic approach can provide a useful
1034 assessment of fault stability, including which of the input variables are the most important for a given
1035 combination of *in situ* stress, fault plane orientation and rock properties. This then enables greater focus on
1036 improving the estimates of the key variables, and the relationships between them. For the Porthtowan Fault
1037 Zone in Cornwall, the modelling in this paper shows that we need more data for, and a better understanding
1038 of the relationship between, coefficients of friction and cohesive strength, especially at low values of friction
1039 (i.e., less than the Byerlee range of 0.6-0.85) to be expected in fault zones. For the South Wales coalfield,
1040 model outputs show how predictions of fault stability can be weighted by a simple index of fault smoothness
1041 to begin to allow for the effects of geometrical weakening within the fault system as whole, rather than
1042 focusing on each individual fault plane taken in isolation.

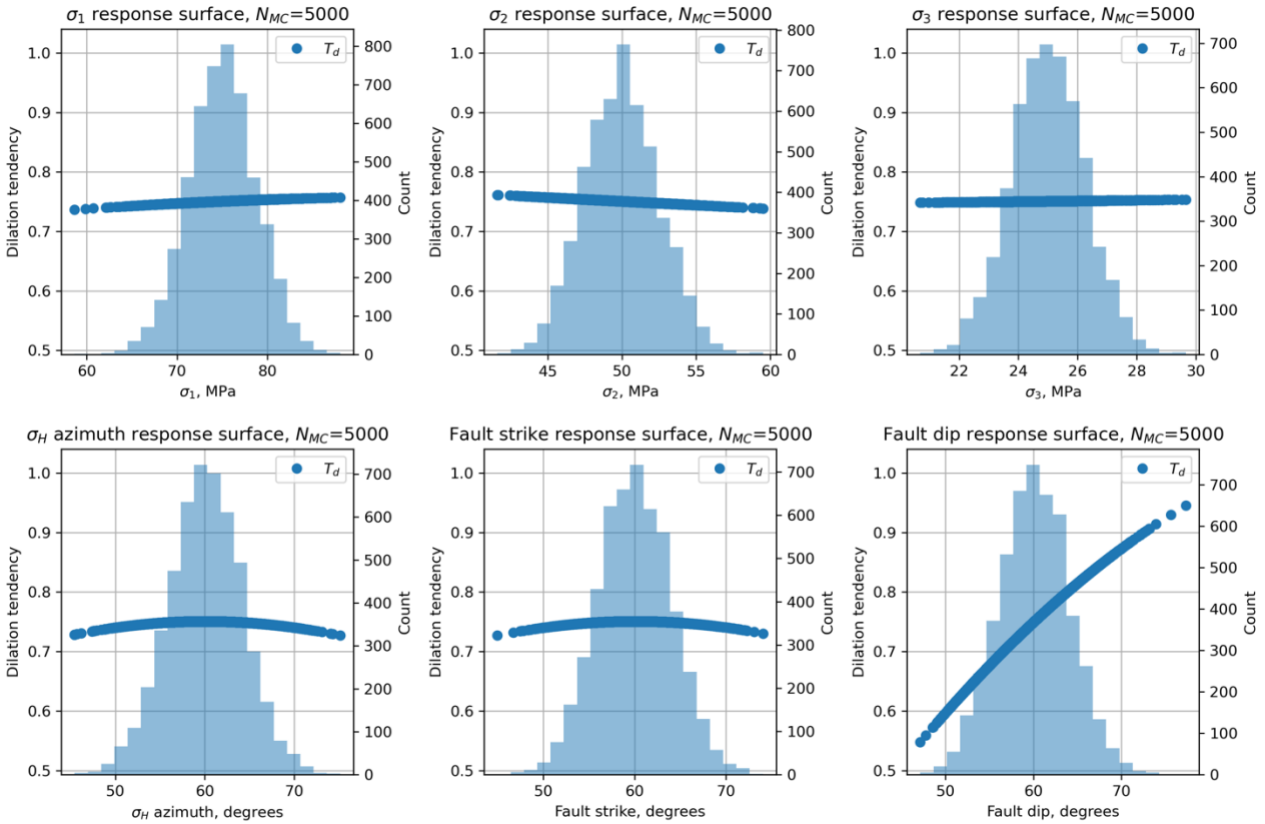
1043 It's obvious that uncertainty in the input parameters must translate into uncertainty in the output
1044 predictions. By combining a Response Surface Methodology with a Monte Carlo approach to the
1045 quantification of fault stability, we can explore, understand, and quantify how differing degrees of
1046 uncertainty among the input parameters feed through to uncertainty in the predicted stability measure.
1047 Response surfaces and tornado plots can help to identify which parameters are the most important in a
1048 particular analysis. Given our current state of knowledge of stress, fault orientations and fault rock
1049 properties, probabilistic estimates and iterative modelling are useful approaches to begin to de-risk the

1050 energy transition. Free, open source software to perform these analyses, such as the Python package pfs,
1051 can help to encourage their wider adoption and further refinement (“given enough eyeballs, all bugs are
1052 shallow”; Raymond, 2001). The deployment of abundant and relatively low-cost citizen science seismometers
1053 (e.g., Raspberry Shakes) could synergise two critical issues: the wider involvement of the public into open
1054 science debates about risk and the simultaneous collection of better data to constrain the local stress field.
1055 The energy transition and decarbonisation are urgent and essential tasks: we will only be successful if we
1056 manage to balance public perceptions of risk with the technical challenges inherent to the exploitation of
1057 faulted rock.

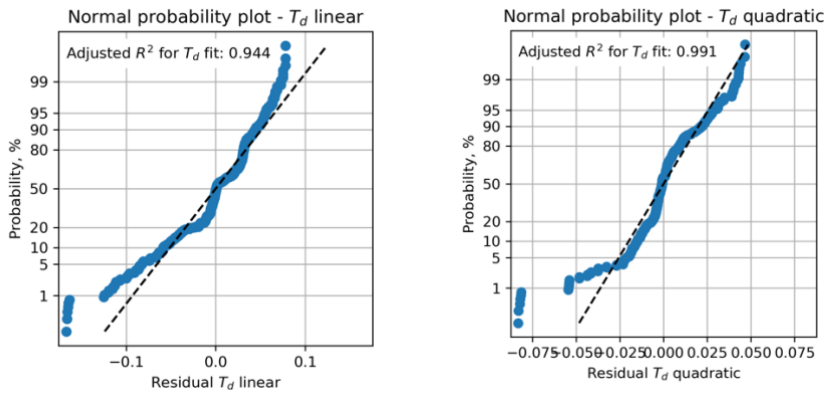
1058

1059 **Appendix A – Dilation tendency plots**

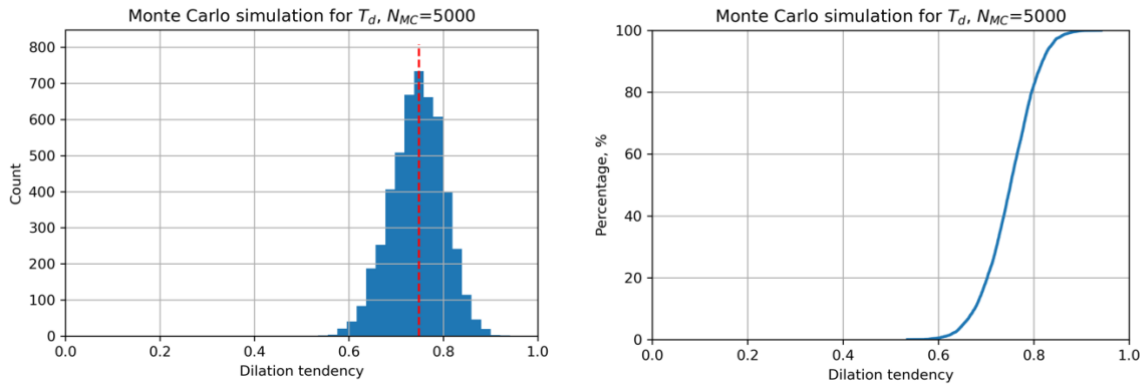
1060 For completeness, we include the analysis of dilation tendency (T_d) for the same synthetic input dataset used
 1061 to calculate slip tendency (T_s) – i.e., input variable distributions taken from Table 2.



1062
 1063 **Figure A1.** Histograms of input variables used to calculate dilation tendency T_d for the synthetic distributions
 1064 shown in Table 2.



1065 **Figure A2.** Residual plots for linear and quadratic response surfaces for dilation tendency using synthetic
 1066 data. The quadratic fit has a higher value of the adjusted R^2 parameter and is therefore deemed better in this
 1067 case.



1068

1069 **Figure A3.** Output from Monte Carlo simulation ($N_{MC}=5,000$) of dilation tendency calculated using a quadratic
 1070 response surface from synthetic input data. **a.** Histogram of calculated dilation tendency values, in this case
 1071 showing a quasi-normal distribution with a mode of ~ 0.75 . **b.** Cumulative distribution function (CDF) of
 1072 calculated dilation tendency values, showing the range in values from ~ 0.5 to ~ 0.9 .

1073

1074 **Code availability**

1075 <https://github.com/DaveHealy-github/pfs>

1076

1077 **Data availability**

1078

1079 **Author contribution**

1080 DH – 80%, SH – 20%. DH originated the study, wrote the code, ran the models. SH contributed seismology
 1081 data and expertise, and contributed to the writing of the text.

1082

1083 **Competing interests**

1084 The authors declare that they have no conflicts of interest.

1085

1086 **Acknowledgements**

1087 DH first presented the core ideas in this paper at the Tectonic Studies Group AGM in Cardiff in 2014, and
 1088 enjoyed discussions there with Dr Jonathan Turner (RWM Ltd). Thanks to former PhD student Dr Sarah
 1089 Weihmann (now at BGR) and co-supervisor Dr Frauke Schaeffer (Wintershall DEA) for discussions about using
 1090 oil industry wireline log data for quantifying geomechanical models. GMT (Wessel et al., 2013) was used for
 1091 the maps. SciPy (Virtanen et al., 2021), Numpy (Harris et al., 2020), and matplotlib (Hunter, 2007) were used
 1092 for the Python pfs code and Allmendinger et al. (2012) for various geomechanical and geometrical algorithms.
 1093 We thank the reviewers for comments that improved the manuscript.

1094

1095 **References**

1096 Alcalde, J., Bond, C.E., Johnson, G., Ellis, J.F. and Butler, R.W., 2017. Impact of seismic image quality on fault
 1097 interpretation uncertainty. GSA Today.

- 1098 Allmendinger, R.W., Cardozo, N. and Fisher, D.M., 2011. Structural geology algorithms: Vectors and tensors.
1099 Cambridge University Press.
- 1100 Anderson, E.M., 1905. The dynamics of faulting. Transactions of the Edinburgh Geological Society, 8(3),
1101 pp.387-402.
- 1102 Anthony, R.E., Ringler, A.T., Wilson, D.C. and Wolin, E., 2019. Do low-cost seismographs perform well enough
1103 for your network? An overview of laboratory tests and field observations of the OSOP Raspberry Shake 4D.
1104 Seismological Research Letters, 90(1), pp.219-228.
- 1105 Ayash, S.C., Dobroskok, A.A., Sorensen, J.A., Wolfe, S.L., Steadman, E.N. and Harju, J.A., 2009. Probabilistic
1106 approach to evaluating seismicity in CO₂ storage risk assessment. Energy Procedia, 1(1), pp.2487-2494.
- 1107 Baptie, B., 2010. Seismogenesis and state of stress in the UK. Tectonophysics, 482(1-4), pp.150-159.
- 1108 Barcelona, H., Yagupsky, D., Vigide, N. and Senger, M., 2019. Structural model and slip-dilation tendency
1109 analysis at the Copahue geothermal system: inferences on the reservoir geometry. Journal of Volcanology
1110 and Geothermal Research, 375, pp.18-31.
- 1111 Batchelor, A.S. and Pine, R.J., 1986, August. The results of in situ stress determinations by seven methods to
1112 depths of 2500 m in the Carnmenellis granite. In ISRM International Symposium. OnePetro.
- 1113 Beamish, D. and Busby, J., 2016. The Cornubian geothermal province: heat production and flow in SW
1114 England: estimates from boreholes and airborne gamma-ray measurements. Geothermal Energy, 4(1), pp.1-
1115 25.
- 1116 Becker, A. and Davenport, C.A., 2001. Contemporary in situ stress determinations at three sites in Scotland
1117 and northern England. Journal of Structural Geology, 23(2-3), pp.407-419.
- 1118 Blenkinsop, T.G., Long, R.E., Kusznir, N.J. and Smith, M.J., 1986. Seismicity and tectonics in Wales. Journal of
1119 the Geological Society, 143(2), pp.327-334.
- 1120 Bond, C.E., 2015. Uncertainty in structural interpretation: Lessons to be learnt. Journal of Structural Geology,
1121 74, pp.185-200.
- 1122 Box, G.E., 1951. Wilson. KB [1951] On the Experimental Attainment of Optimum Conditions. Journal of the
1123 Royal Statistical Society, Series B (Methodological), 13(1), pp.1-45.
- 1124 Caine, J.S., Evans, J.P. and Forster, C.B., 1996. Fault zone architecture and permeability structure. Geology,
1125 24(11), pp.1025-1028.
- 1126 Carvell, J., Blenkinsop, T., Clarke, G. and Tonelli, M., 2014. Scaling, kinematics and evolution of a polymodal
1127 fault system: Hail Creek Mine, NE Australia. Tectonophysics, 632, pp.138-150.
- 1128 Chang, C., Zoback, M.D. and Khaksar, A., 2006. Empirical relations between rock strength and physical
1129 properties in sedimentary rocks. Journal of Petroleum Science and Engineering, 51(3-4), pp.223-237.
- 1130 Chiaramonte, L., Zoback, M.D., Friedmann, J. and Stamp, V., 2008. Seal integrity and feasibility of CO₂
1131 sequestration in the Teapot Dome EOR pilot: geomechanical site characterization. Environmental Geology,
1132 54(8), pp.1667-1675.
- 1133 Clarke, H., Verdon, J.P., Kettlety, T., Baird, A.F. and Kendall, J.M., 2019. Real-time imaging, forecasting, and
1134 management of human-induced seismicity at Preston New Road, Lancashire, England. Seismological
1135 Research Letters, 90(5), pp.1902-1915.
- 1136 Cochran, E.S., 2018. To catch a quake. Nature communications, 9(1), pp.1-4.
- 1137 CCC (UK Committee on Climate Change), 2019. Net Zero—Technical Report.

- 1138 Cuss, R.J., Rutter, E.H. and Holloway, R.F., 2003. The application of critical state soil mechanics to the
1139 mechanical behaviour of porous sandstones. *International Journal of Rock Mechanics and Mining Sciences*,
1140 40(6), pp.847-862.
- 1141 Das, D. and Mallik, J., 2020. Koyna earthquakes: a review of the mechanisms of reservoir-triggered seismicity
1142 and slip tendency analysis of subsurface faults. *Acta Geophysica*, pp.1-16.
- 1143 Elsworth, D., Spiers, C.J. and Niemeijer, A.R., 2016. Understanding induced seismicity. *Science*, 354(6318),
1144 pp.1380-1381.
- 1145 Farr, G., Sadasivam, S., Watson, I.A., Thomas, H.R. and Tucker, D., 2016. Low enthalpy heat recovery potential
1146 from coal mine discharges in the South Wales Coalfield. *International Journal of Coal Geology*, 164, pp.92-
1147 103.
- 1148 Farr, G., Busby, J., Wyatt, L., Crooks, J., Schofield, D.I. and Holden, A., 2021. The temperature of Britain's
1149 coalfields. *Quarterly Journal of Engineering Geology and Hydrogeology*, 54(3).
- 1150 Faulkner, D.R., Jackson, C.A.L., Lunn, R.J., Schlische, R.W., Shipton, Z.K., Wibberley, C.A.J. and Withjack, M.O.,
1151 2010. A review of recent developments concerning the structure, mechanics and fluid flow properties of fault
1152 zones. *Journal of Structural Geology*, 32(11), pp.1557-1575.
- 1153 Fellgett, M.W., Kingdon, A., Williams, J.D. and Gent, C.M., 2018. Stress magnitudes across UK regions: New
1154 analysis and legacy data across potentially prospective unconventional resource areas. *Marine and
1155 Petroleum Geology*, 97, pp.24-31.
- 1156 Fellgett, M.W. and Haslam, R., 2021, April. Fractures in Granite: Results from United Downs Deep Geothermal
1157 well UD-1. In *EGU General Assembly Conference Abstracts* (pp. EGU21-5593).
- 1158 Ferrill, D.A., Winterle, J., Wittmeyer, G., Sims, D., Colton, S., Armstrong, A. and Morris, A.P., 1999. Stressed
1159 rock strains groundwater at Yucca Mountain, Nevada. *GSA Today*, 9(5), pp.1-8.
- 1160 Goebel, T.H.W., Rosson, Z., Brodsky, E.E. and Walter, J.I., 2019. Aftershock deficiency of induced earthquake
1161 sequences during rapid mitigation efforts in Oklahoma. *Earth and Planetary Science Letters*, 522, pp.135-143.
- 1162 Green, A.S.P., Baria, R., Madge, A. and Jones, R., 1988. Fault-plane analysis of microseismicity induced by
1163 fluid injections into granite. *Geological Society, London, Engineering Geology Special Publications*, 5(1),
1164 pp.415-422.
- 1165 Hackston, A. and Rutter, E., 2016. The Mohr–Coulomb criterion for intact rock strength and friction—a re-
1166 evaluation and consideration of failure under polyaxial stresses. *Solid Earth*, 7(2), pp.493-508.
- 1167 Hardebeck, J. L., & Shearer, P. M., 2002. A new method for determining first-motion focal
1168 mechanisms. *Bulletin of the Seismological Society of America*, 92(6), 2264-2276.
- 1169 Harris, C.R., Millman, K.J., van der Walt, S.J., Gommers, R., Virtanen, P., Cournapeau, D., Wieser, E., Taylor,
1170 J., Berg, S., Smith, N.J. and Kern, R., 2020. Array programming with NumPy. *Nature*, 585(7825), pp.357-362.
- 1171 Healy, D., Rizzo, R.E., Cornwell, D.G., Farrell, N.J., Watkins, H., Timms, N.E., Gomez-Rivas, E. and Smith, M.,
1172 2017. FracPaQ: A MATLAB™ toolbox for the quantification of fracture patterns. *Journal of Structural Geology*,
1173 95, pp.1-16.
- 1174 Heidbach, O., Rajabi, M., Cui, X., Fuchs, K., Müller, B., Reinecker, J., Reiter, K., Tingay, M., Wenzel, F., Xie, F.
1175 and Ziegler, M.O., 2018. The World Stress Map database release 2016: Crustal stress pattern across scales.
1176 *Tectonophysics*, 744, pp.484-498.
- 1177 Hennings, P.H., Lund Snee, J.E., Osmond, J.L., DeShon, H.R., Dommissive, R., Horne, E., Lemons, C. and Zoback,
1178 M.D., 2019. Injection-induced seismicity and fault-slip potential in the Fort Worth Basin, Texas. *Bulletin of
1179 the Seismological Society of America*, 109(5), pp.1615-1634.

- 1180 Hicks, S. P., Verdon, J., Baptie, B., Lockett, R., Mildon, Z. K., & Gernon, T., 2019. A shallow earthquake swarm
1181 close to hydrocarbon activities: Discriminating between natural and induced causes for the 2018–2019
1182 Surrey, United Kingdom, earthquake sequence. *Seismological Research Letters*, 90(6), 2095–2110.
- 1183 Hicks, S., Goes, S., Whittaker, A. C., & Stafford, P. J., 2021. Multivariate statistical appraisal of regional
1184 susceptibility to induced seismicity: application to the Permian Basin, SW United States. *EarthArXiv*.
1185 <https://doi.org/10.31223/X5NW3D>
- 1186 Hincks, T., Aspinall, W., Cooke, R. and Gernon, T., 2018. Oklahoma's induced seismicity strongly linked to
1187 wastewater injection depth. *Science*, 359(6381), pp.1251-1255.
- 1188 Holmgren, J.M. and Werner, M.J., 2021. Raspberry Shake Instruments Provide Initial Ground-Motion
1189 Assessment of the Induced Seismicity at the United Downs Deep Geothermal Power Project in Cornwall,
1190 United Kingdom. *The Seismic Record*, 1(1), pp.27-34.
- 1191 Hunter, J.D., 2007. Matplotlib: A 2D graphics environment. *Computing in science & engineering*, 9(03), pp.90-
1192 95.
- 1193 IPCC, 2018. *In: Masson-Delmotte, V., Zhai, P., Pörtner, H.O., Roberts, D., Skea, J., Shukla, P.R., Pirani, A.,
1194 Moufouma-Okia, W., Péan, C., Pidcock, R. and Connors, S., 2018. Global warming of 1.5 C. An IPCC Special
1195 Report on the impacts of global warming of, 1, pp.1-9.*
- 1196 Jaeger, J.C., Cook, N.G. and Zimmerman, R., 2009. *Fundamentals of rock mechanics*. John Wiley & Sons.
- 1197 Jacquey, A.B., Cacace, M., Blöcher, G. and Scheck-Wenderoth, M., 2015. Numerical investigation of
1198 thermoelastic effects on fault slip tendency during injection and production of geothermal fluids. *Energy
1199 Procedia*, 76, pp.311-320.
- 1200 Kingdon, A., Fellgett, M.W. and Williams, J.D., 2016. Use of borehole imaging to improve understanding of
1201 the in-situ stress orientation of Central and Northern England and its implications for unconventional
1202 hydrocarbon resources. *Marine and Petroleum Geology*, 73, pp.1-20.
- 1203 Ledingham, P., Cotton, L. and Law, R., 2019, February. The united downs deep geothermal power project. In
1204 *Proceedings of the 44th Workshop on Geothermal Reservoir Engineering*, Stanford University, Stanford, CA,
1205 USA (pp. 11-13).
- 1206 Leonard, M., 2010. Earthquake fault scaling: Self-consistent relating of rupture length, width, average
1207 displacement, and moment release. *Bulletin of the Seismological Society of America*, 100(5A), pp.1971-1988.
- 1208 Li, X., Main, I. and Jupe, A., 2018. Induced seismicity at the UK 'hot dry rock' test site for geothermal energy
1209 production. *Geophysical Journal International*, 214(1), pp.331-344.
- 1210 Lisle, R.J. and Srivastava, D.C., 2004. Test of the frictional reactivation theory for faults and validity of fault-
1211 slip analysis. *Geology*, 32(7), pp.569-572.
- 1212 McLennan, D., Noble, S., Noble, M., Plunkett, E., Wright, G. and Gutacker, N., 2019. *The English indices of
1213 deprivation 2019: Technical report*.
- 1214 Miocic, J.M., Johnson, G. and Bond, C.E., 2019. Uncertainty in fault seal parameters: implications for CO₂
1215 column height retention and storage capacity in geological CO₂ storage projects. *Solid earth*, 10(3), pp.951-
1216 967.
- 1217 Moeck, I., Kwiatek, G. and Zimmermann, G., 2009. Slip tendency analysis, fault reactivation potential and
1218 induced seismicity in a deep geothermal reservoir. *Journal of Structural Geology*, 31(10), pp.1174-1182.
- 1219 Moos, D., Peska, P., Finkbeiner, T. and Zoback, M., 2003. Comprehensive wellbore stability analysis utilizing
1220 quantitative risk assessment. *Journal of Petroleum Science and Engineering*, 38(3-4), pp.97-109.
- 1221 Morris, A., Ferrill, D.A. and Henderson, D.B., 1996. Slip-tendency analysis and fault reactivation. *Geology*,
1222 24(3), pp.275-278.

- 1223 Musson, R.M., 1996. The seismicity of the British Isles. *Annals of Geophysics*, 39(3).
- 1224 Myers, R.H., Montgomery, D.C. and Anderson-Cook, C.M., 2016. Response surface methodology: process and
1225 product optimization using designed experiments. John Wiley & Sons.
- 1226 Nolan, L., 2016, July. The Welsh Index of Multiple Deprivation. In Presentation for the GSS Methodology
1227 Conference (Vol. 6).
- 1228 Pine, R.J. and Batchelor, A.S., 1984, October. Downward migration of shearing in jointed rock during hydraulic
1229 injections. In *International Journal of Rock Mechanics and Mining Sciences & Geomechanics Abstracts* (Vol.
1230 21, No. 5, pp. 249-263). Pergamon.
- 1231 Raleigh, C.B., Healy, J.H. & Bredehoeft, J.D., 1976. An experiment in earthquake control at Rangely, Colorado.
1232 *Science*, 191(4233), pp.1230-1237.
- 1233 Raymond, E., 2001. *The Cathedral & the Bazaar*, Revised Edition. O'Reilly.
- 1234 Reinecker, J., Gutmanis, J., Foxford, A., Cotton, L., Dalby, C. and Law, R. Geothermal exploration and
1235 reservoir modelling of the united downs deep geothermal project, Cornwall (UK). *Geothermics*, 97,
1236 p.102226, 2021.
- 1237 Roberts, J. J., Bond, C. E., & Shipton, Z. K., 2021. Fracking bad language—hydraulic fracturing and earthquake
1238 risks. *Geoscience Communication*, 4(2), 303-327.
- 1239 Rohmer, J. and Bouc, O., 2010. A response surface methodology to address uncertainties in cap rock failure
1240 assessment for CO₂ geological storage in deep aquifers. *International Journal of Greenhouse Gas Control*,
1241 4(2), pp.198-208.
- 1242 Rutter, E.H. and Hadizadeh, J., 1991. On the influence of porosity on the low-temperature brittle—ductile
1243 transition in siliciclastic rocks. *Journal of Structural Geology*, 13(5), pp.609-614.
- 1244 Sanchez, C., Saldi, G., Mitchell, T., Iacoviello, F., Meredith, P., Jones, A., Oelkers, E., and Striolo, A., 2020. The
1245 role of fluid chemistry on permeability and fault strength evolution in granite, EGU General Assembly 2020,
1246 Online, 4–8 May 2020, EGU2020-21850, <https://doi.org/10.5194/egusphere-egu2020-21850>
- 1247 Sanchez-Roa, C., Saldi, G.D., Mitchell, T.M., Iacoviello, F., Bailey, J., Shearing, P.R., Oelkers, E.H., Meredith,
1248 P.G., Jones, A.P. and Striolo, A., 2021. The role of fluid chemistry on permeability evolution in granite:
1249 Applications to natural and anthropogenic systems. *Earth and Planetary Science Letters*, 553, p.116641.
- 1250 Stephenson, M.H., Ringrose, P., Geiger, S., Bridden, M. and Schofield, D., 2019. Geoscience and
1251 decarbonization: current status and future directions. *Petroleum Geoscience*, 25(4), pp.501-508.
- 1252 Stirling, M.W., Wesnousky, S.G. and Shimazaki, K., 1996. Fault trace complexity, cumulative slip, and the
1253 shape of the magnitude-frequency distribution for strike-slip faults: A global survey. *Geophysical Journal
1254 International*, 124(3), pp.833-868.
- 1255 Streit, J.E. and Hillis, R.R., 2004. Estimating fault stability and sustainable fluid pressures for underground
1256 storage of CO₂ in porous rock. *Energy*, 29(9-10), pp.1445-1456.
- 1257 Townend, J. and Zoback, M.D., 2000. How faulting keeps the crust strong. *Geology*, 28(5), pp.399-402.
- 1258 Verdon, J.P. and Budge, J., 2018. Examining the capability of statistical models to mitigate induced seismicity
1259 during hydraulic fracturing of shale gas reservoirs. *Bulletin of the Seismological Society of America*, 108(2),
1260 pp.690-701.
- 1261 Virtanen, P., Gommers, R., Oliphant, T.E., Haberland, M., Reddy, T., Cournapeau, D., Burovski, E., Peterson,
1262 P., Weckesser, W., Bright, J. and Van Der Walt, S.J., 2020. SciPy 1.0: fundamental algorithms for scientific
1263 computing in Python. *Nature methods*, 17(3), pp.261-272.
- 1264 Walker, A., Baptie, B. and Ottemoller, L., 2003. UK earthquake monitoring 2002/2003.

- 1265 Walsh III, F.R. and Zoback, M.D., 2016. Probabilistic assessment of potential fault slip related to injection-
1266 induced earthquakes: Application to north-central Oklahoma, USA. *Geology*, 44(12), pp.991-994.
- 1267 Walsh, J.J., Childs, C., Meyer, V., Manocchi, T., Imber, J., Nicol, A., Tuckwell, G., Bailey, W.R., Bonson, C.G.,
1268 Watterson, J. & Nell, P.A., 2001. Geometric controls on the evolution of normal fault systems. *Geological*
1269 *Society, London, Special Publications*, 186(1), pp.157-170.
- 1270 Wang, Q., Ru, Z., Zhao, R., Yu, C., Liu, Y. & Deng, S., 2020. A study on permeability along strike slip faults in
1271 Shunbei reservoir of Tarim Basin, China. *Energy Sources, Part A: Recovery, Utilization, and Environmental*
1272 *Effects*, pp.1-17.
- 1273 Wells, D.L. & Coppersmith, K.J., 1994. New empirical relationships among magnitude, rupture length, rupture
1274 width, rupture area, and surface displacement. *Bulletin of the seismological Society of America*, 84(4),
1275 pp.974-1002.
- 1276 Wesnousky, S.G., 1988. Seismological and structural evolution of strike-slip faults. *Nature*, 335(6188), pp.340-
1277 343.
- 1278 Wessel, P., Smith, W.H., Scharroo, R., Luis, J. and Wobbe, F., 2013. Generic mapping tools: improved version
1279 released. *Eos, Transactions American Geophysical Union*, 94(45), pp.409-410.
- 1280 Wibberley, C.A., Yielding, G. and Di Toro, G., 2008. Recent advances in the understanding of fault zone
1281 internal structure: a review. *Geological Society, London, Special Publications*, 299(1), pp.5-33.
- 1282 Williams, J.D., Fellgett, M.W. and Quinn, M.F., 2016. Carbon dioxide storage in the Captain Sandstone aquifer:
1283 determination of in situ stresses and fault-stability analysis. *Petroleum Geoscience*, 22(3), pp.211-222.
- 1284 Williams, J.D.O., Gent, C.M.A., Fellgett, M.W. and Gamboa, D., 2018. Impact of in situ stress and fault
1285 reactivation on seal integrity in the East Irish Sea Basin, UK. *Marine and Petroleum Geology*, 92, pp.685-696.
- 1286 Zhao, J., 1987. Experimental studies of the hydro-thermo-mechanical behaviour of joints in granite. Unpubl.
1287 PhD thesis, Imperial College, London, UK.
- 1288